

AD-A178 858

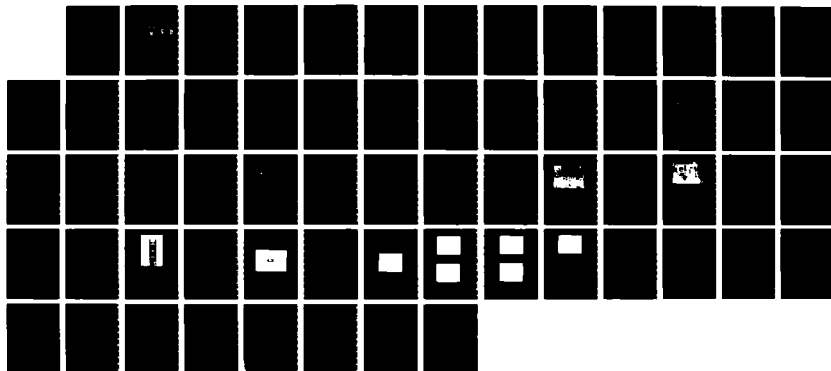
FREQUENCY SPECTRUM OF SOFT X-RAY EMISSION FROM
TRANSISTOR RADIATION(U) NAVAL POSTGRADUATE SCHOOL
MONTEREY CA S K YOON DEC 86

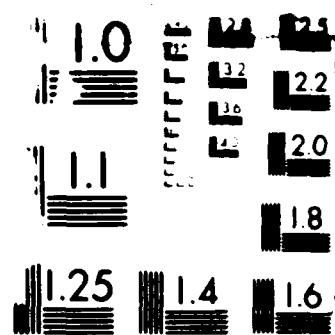
1/1

UNCLASSIFIED

F/G 7/4

ML





AD-A178 858

NAVAL POSTGRADUATE SCHOOL

Monterey, California



DTIC
ELECTE
APR 08 1987
S D

THESIS

FREQUENCY SPECTRUM OF SOFT X-RAY
EMISSION
FROM
TRANSITION RADIATION

by

Yoon, Seog Koo

December 1986

Thesis Advisor

John R. Neighbours

Approved for public release; distribution is unlimited.

REPORT DOCUMENTATION PAGE

1a REPORT SECURITY CLASSIFICATION UNCLASSIFIED			1b RESTRICTIVE MARKINGS		
2a SECURITY CLASSIFICATION AUTHORITY			3 DISTRIBUTION/AVAILABILITY OF REPORT Approved for public release; distribution is unlimited.		
2b DECLASSIFICATION/DOWNGRADING SCHEDULE					
4 PERFORMING ORGANIZATION REPORT NUMBER(S)			5 MONITORING ORGANIZATION REPORT NUMBER(S)		
6a NAME OF PERFORMING ORGANIZATION Naval Postgraduate School		6b OFFICE SYMBOL (if applicable) 61	7a NAME OF MONITORING ORGANIZATION Naval Postgraduate School		
6c ADDRESS (City, State, and ZIP Code) Monterey, California 93943-5000			7b ADDRESS (City, State, and ZIP Code) Monterey, California 93943-5000		
8a NAME OF FUNDING/SPONSORING ORGANIZATION		8b OFFICE SYMBOL (if applicable)	9 PROCUREMENT INSTRUMENT IDENTIFICATION NUMBER		
8c ADDRESS (City, State, and ZIP Code)			10 SOURCE OF FUNDING NUMBERS		
			PROGRAM ELEMENT NO	PROJECT NO	TASK NO
			WORK UNIT ACCESSION NO		
11 TITLE (Include Security Classification) FREQUENCY SPECTRUM OF SOFT X-RAY EMISSION FROM TRANSITION RADIATION					
12 PERSONAL AUTHOR(S) Yoon, Seog Koo					
13a TYPE OF REPORT Master's Thesis		13b TIME COVERED FROM TO		14 DATE OF REPORT (Year, Month, Day) 1986 December	
				15 PAGE COUNT 61	
16 SUPPLEMENTARY NOTATION					
17 COSATI CODES			18 SUBJECT TERMS (Continue on reverse if necessary and identify by block number)		
FIELD	GROUP	SUB-GROUP	Transition Radiation; Radiation Cone; Coherence;		
			Differential Production Efficiency; Absorption. <—		
19 ABSTRACT (Continue on reverse if necessary and identify by block number)					
<p>The absolute differential production efficiencies from foil stack materials for an electron-beam energy of 65 MeV were measured. The spectra shapes and the absolute differential production efficiencies for each of the four foil stacks are well matched by the calculated values. The transition radiation cone was measured using a motor-driven detector. The measured apex angle is in agreement with the optimum radiation cone angle. Aluminum bandwidth narrowing associated with K-edge absorption was observed. The production intensity was compared with the theoretical prediction and interpreted in terms of absorption and coherence.</p>					
20 DISTRIBUTION/AVAILABILITY OF ABSTRACT <input checked="" type="checkbox"/> UNCLASSIFIED/UNLIMITED <input type="checkbox"/> SAME AS RPT <input type="checkbox"/> DTIC USERS			21 ABSTRACT SECURITY CLASSIFICATION Unclassified		
22a NAME OF RESPONSIBLE INDIVIDUAL John R. Neighbours			22b TELEPHONE (Include Area Code) (408) 646-2922		22c OFFICE SYMBOL 61Nb

Approved for public release; distribution is unlimited.

Frequency Spectrum of Soft X-ray Emission
from
Transition Radiation

by

Yoon, Seog Koo
Major, Republic of Korea Army
B.S., Korea Military Academy, 1978

Submitted in partial fulfillment of the
requirements for the degree of

MASTER OF SCIENCE IN PHYSICS

from the

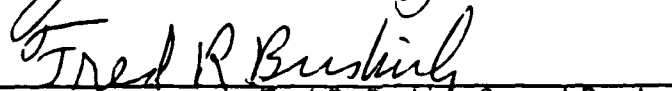
NAVAL POSTGRADUATE SCHOOL
December 1986

Author:



Yoon, Seog Koo

Approved by:


John R. Neighbours, Thesis Advisor


Fred R. Buskirk, Second Reader


G. E. Schacher, Chairman,
Department of Physics


John N. Dyer,
Dean of Science and Engineering

ABSTRACT

The absolute differential production efficiencies from foil stack materials for an electron-beam energy of 65 MeV were measured. The spectra shapes and the absolute differential production efficiencies for each of the four foil stacks are well matched by the calculated values. The transition radiation cone was measured using a motor-driven detector. The measured apex angle is in agreement with the optimum radiation cone angle. Aluminum bandwidth narrowing associated with K-edge absorption was observed. The production intensity was compared with the theoretical prediction and interpreted in terms of absorption and coherence.



Accession For	
NTIS	CRA&I <input checked="" type="checkbox"/>
ERIC	TAB <input type="checkbox"/>
Unannounced	<input type="checkbox"/>
Justification	
By	
Distribution/	
Availability Codes	
Dist	Avail and/or Special
A-1	

TABLE OF CONTENTS

I.	INTRODUCTION	9
II.	THEORY	10
A.	IN-PHASE ADDITION OF THE TRANSITION RADIATION	10
B.	TRANSITION RADIATION CONE	14
C.	COMPUTER SPECTRUM ANALYSIS	16
1.	Formation Length	16
2.	Single Interface Intensity	18
3.	Single Foil Interference Factor	19
4.	Multi-foil Interference Factor	20
5.	Shape of the Transition Radiation	22
III.	EXPERIMENTAL APPARATUS	33
A.	EXPERIMENTAL CONCEPT	33
B.	EQUIPMENT PERFORMANCE	34
1.	Linac	34
2.	Target and Detector Chamber	35
3.	Gas Flow System	35
4.	Detection Apparatus	36
5.	Observation Station	40
6.	Stack Foils Used during Experiment	41
IV.	RESULTS AND CONCLUSIONS	45
A.	RESULTS	45
B.	CONCLUSIONS	50
APPENDIX A:	ELECTRON LINEAR ACCELERATOR PARAMETERS	52
APPENDIX B:	CALCULATION OF PLASMA FREQUENCY	53
APPENDIX C:	MASS ATTENUATION COEFFICIENTS FOR PHOTONS IN AL AND MYLAR	55
APPENDIX D:	BASIC PROGRAM (HP COMPUTER)	57
	LIST OF REFERENCES	59
	INITIAL DISTRIBUTION LIST	60

LIST OF TABLES

1. MEASUREMENTS OF TOTAL COUNTS	45
2. COMPARISON OF RADIATION CONE ANGLE AT 65 MEV	46
3. COMPARISON BETWEEN CALCULATED AND MEASURED DATA	49
4. LINAC PARAMETER	52
5. PLASMA FREQUENCY	53

LIST OF FIGURES

2.1	Schematic Diagram of a Multi-foil Radiator	11
2.2	Condition for Coherent Phase Summation	13
2.3	Schematic Diagram of the Transition Radiation Cone	14
2.4	Coherent and Incoherent Transition Radiation from a Foil Stack	15
2.5	Formation Length of Vacuum ($E_1 = 0$, $\gamma = 127$, $\theta \sim 1/\gamma$)	17
2.6	Formation Length of Al ($E_2 = 32.8$ eV, $\gamma = 127$, $\theta \sim 1/\gamma$)	18
2.7	Formation Length of Mylar ($E_2 = 19.9$ eV, $\gamma = 127$, $\theta \sim 1/\gamma$)	19
2.8	Single Interface Factor of Al ($\gamma = 127$)	20
2.9	Single Interface Factor of Mylar ($\gamma = 127$)	21
2.10	Single Foil Interference Factor of Al ($\ell_2 = 1\mu\text{m}$)	22
2.11	Single Foil Interference Factor of Mylar ($\ell_2 = 2.5\mu\text{m}$)	23
2.12	Single Foil Interference Dependence on Foil Thickness in Mylar ($E_2 = 19.9$ eV)	24
2.13	Effect of the Number of Foil on the Multi-foil Factor ($\sigma = 0.001$)	25
2.14	Multi-foil Absorption Factor of Mylar ($M = 8$, $\ell_2 = 2.5\mu\text{m}$)	26
2.15	Absorption Factor of Mylar (Single Interface x Multi-foil Absorption)	27
2.16	Calculated Differential Production Efficiency from 30 Foils $1\mu\text{m}$ Al	28
2.17	Calculated Differential Production Efficiency from 8 Foils $2.5\mu\text{m}$ Mylar	29
2.18	Calculated Differential Production Efficiency from 1 Foil $26\mu\text{m}$ Al	30
2.19	Calculated Differential Production Efficiency from 1 Foil $19\mu\text{m}$ Mylar	30
2.20	Calculated Spectral Distribution from 8 Foils of Various Thickness of Mylar for 65 MeV	31
2.21	Effect of the Number of Foils on the Radiation Peak of the $1\mu\text{m}$ Al	31
2.22	Calculated Effect of K-shell Absorption on the Al Spectrum for 65 MeV Electron	32
3.1	Schematic Diagram of a Experimental Apparatus	33
3.2	Schematic Diagram of a Linear Accelerator	34
3.3	Target and Detector Chamber	35
3.4	Schematic Diagram of a Gas Flow System	36
3.5	Detection Apparatus	37
3.6	Manson Model 04 Gas Flow Proportional Counter	38
3.7	Electrical Field Strength and Potential vs. Radius	39
3.8	Proportional Counter Efficiency	40

3.9	Block Diagram of the Data-collection Electronics	41
3.10	Stack Foils Used during Experiment	42
3.11	Design of Mylar Coherent Stack	43
3.12	Mylar Coherent Stack	44
4.1	Fe ⁵⁵ Spectrum in 400 Torr	46
4.2	Measured Pulse Height Counts from 30 Foils 1 μ m Al with Bremsstrahlung	47
4.3	Comparison of Measured Pulse Height Counts from 30 Foils 1 μ m and 1 Foil 26 μ m Al	47
4.4	Fe ⁵⁵ Spectrum in 350 Torr	48
4.5	Measured Pulse Height Counts from 8 Foils 2.5 μ m Mylar with Bremsstrahlung	48
4.6	Measured Pulse Height Counts from 1 Foil 19 μ m Mylar	49
C.1	Mass Attenuation Coefficient for Photons in Al	55
C.2	Mass Attenuation Coefficient for Photons in Mylar	56

ACKNOWLEDGEMENTS

I would like to express my thanks for the support and guidance given by my thesis advisor, Professor J. R. Neighbours, and my second reader Professor F. R. Buskirk in completing this thesis. I would also like to thank Dr. M. A. Piestrup for the equipment and suggestions concerning the experiment, as well as Mr. D. Snyder for the linac operation. A very special thanks to my wife, Hee Jae for her patience during these two and half years.

I. INTRODUCTION

In 1946 V. L. Ginsburg and I. M. Frank predicted the existence of transition radiation [Ref. 1: pp.353-362]. This effect was discovered during a period in which Russian theoreticians made an extensive effort in the area of radiation producing phenomena after the discovery of the Cerenkov effect. Actually, transition radiation can be considered, from a phenomenological point of view, as a Cerenkov effect of the second order since it occurs when a charged particle crosses the boundary between two media with differing dielectric constants. More generally, this effect will take place in the presence of the inhomogeneities in the medium.

Through the years, experimental investigation devoted to this effect were undertaken primarily with nonrelativistic electrons, in order to firmly establish the validity of the theory, in spite of inconvenience arising at these low energies from the simultaneous existence of scattering of the electrons and of bremsstrahlung radiation. Interest in this type of radiation was renewed after G. M. Garibyan predicted that the transition radiation yield was proportional to the energy of the particle. The application of this property to the detection and identification of individual particles was the main goal of high energy physics instrumentation, cosmic rays, and astrophysics.

In recent years the in-phase addition of radiation from multiple boundaries has been predicted and observed [Ref. 2: p.3594]. For a single interface, the radiation yield produced by an individual electron is very weak; of the order of the fine-structure constant *i. e.*, roughly one photon for a hundred electrons. For *M* boundaries the spectral intensity varies as M^2 , so that the emission can be much greater than for a single interface. In this thesis the effects of light absorption, and random variation in foil thickness are included in the design of transition radiation sources for the generation of x-rays. The foil dimensions must be held to close tolerance in order to satisfy the coherence conditions from each boundary.

II. THEORY

A. IN-PHASE ADDITION OF THE TRANSITION RADIATION

Transition radiation occurs when a moving charged particle encounters a sudden change in dielectric constant at the interface between different media (e.g., between a vacuum and a solid). Ordinarily, a particle which moves with constant velocity does not radiate unless it is in a refractive medium and the particle exceeds the velocity of the electromagnetic wave in medium -- as is the case for Cerenkov radiation. However, if the interaction length is limited , or equivalently, if the dielectric constant changes suddenly, then velocity matching is not important. The minimum distance over which an electromagnetic wave and a charged particle can exchange energy is called the "*formation length*" and is given by [Ref. 3: pp. 40-44]

$$Z_i = \frac{2c\beta}{\omega(1-\beta\sqrt{\epsilon_i}\sin\theta)}, \quad (2.1)$$

where $\gamma = (1-\beta^2)^{-1/2}$, ϵ_i ($i=1, 2$) = $1 - (\omega_i/\omega)^2$ are the dielectric constants of the two media, ω_i are their respective plasma frequencies, $\beta = v/c$, v is the speed of the electron, c is the speed of light, $\hbar\omega$ is the photon energy, and θ is the angle of emission. For relativistic electrons $\beta \sim 1$, $\sin\theta \sim \theta$, and $1/\gamma^2 \sim 2(1-\beta)$, so that

$$Z_i \sim \frac{4\lambda\beta}{(1/\gamma^2) + \theta^2 + (\omega_i/\omega)^2}, \quad (2.2)$$

where $\lambda = c/\omega$.

In traversing an interface, the number of photons per unit time emitted by an electron is proportional to the dot product of the particle velocity and electric field strength. For a single interface V. L. Ginzburg and I. M. Frank calculated the differential production efficiency for transition radiation as [Ref. 1: p.353]

$$\frac{d^2N_o}{d\Omega d\omega} = \left[\frac{\alpha\theta^2\omega}{16\pi^2c^2} \right] (Z_1 - Z_2)^2, \quad (2.3)$$

where $d^2N_0/d\Omega d\omega$ is the number of photons emitted per frequency per solid angle by a single particle crossing a single dielectric interface, $\alpha = 1/137$ is the fine-structure constant, Ω is the solid angle in steradians, and Z_1 and Z_2 are given by Eq. (2.1).

The spectral intensity from an electron crossing M foil pairs perpendicularly, each composed of two materials of thickness ℓ_1 and ℓ_2 can be calculated by considering the field amplitudes at some observation point [Fig. (2.1)]. The results should be simply the coherent sum of the radiation amplitudes from $2M$ single interfaces. The phase factor must be properly included, taking into account that the particle traverses different interfaces at different times.

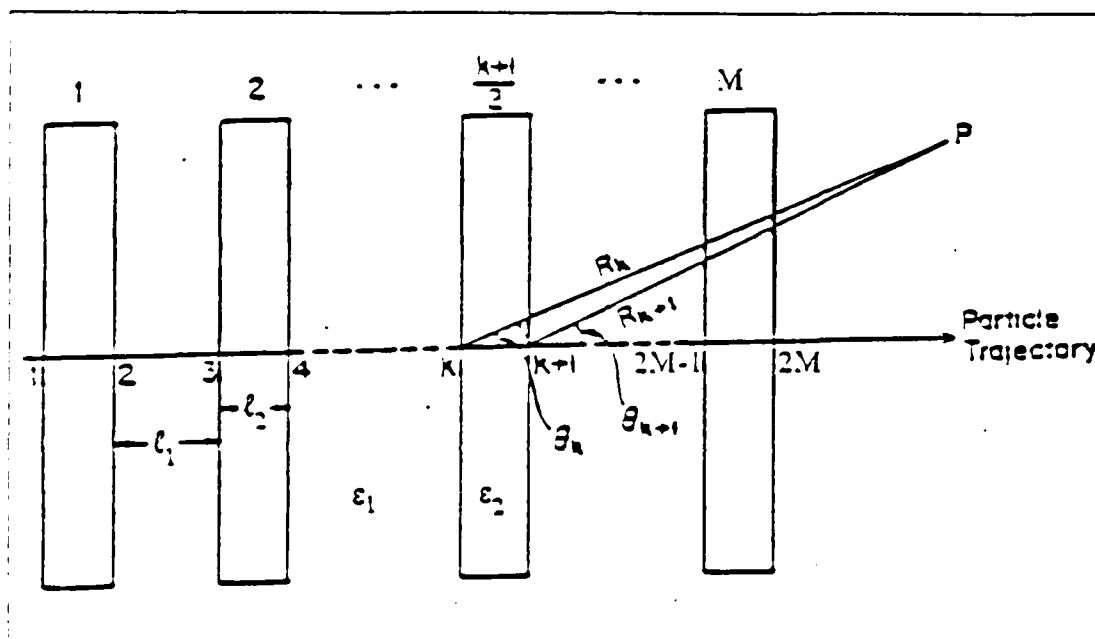


Figure 2.1 Schematic Diagram of a Multi-foil Radiator.

This spectral production efficiency is given by [Ref. 4: p. 23]

$$\frac{d^2N}{d\Omega d\omega} = \left[\frac{d^2N_0}{d\Omega d\omega} \right] 4\sin^2(\ell_2 Z_2) F(M, X), \quad (2.4)$$

where

$$F(M, X) = \frac{1 + \exp(-M\sigma) - 2\exp(-M\sigma/2)\cos(2MX)}{1 + \exp(-\sigma) - 2\exp(-\sigma/2)\cos(2X)}, \quad (2.5)$$

where N is the number of photons emitted by a single particle traveling through a dielectric stack, where $\sigma = \mu_1 \ell_1 + \mu_2 \ell_2$, $X = \ell_1/Z_1 + \ell_2/Z_2$, and μ_1 and μ_2 are the linear absorption coefficients of the spacing and foil media, respectively ($\mu_1 \sim 0$ for vacuum spacing). When the periods of $F(M,X)$ are not experimentally resolvable and the photon absorption of radiation is not small, Eq. (2.5) becomes [Ref. 5: p.918]

$$\langle F(M,X) \rangle \sim \frac{1 - \exp(-M\sigma)}{\sigma} \quad (2.6)$$

At high photon energies, where x-ray absorption is small or negligible, so that ($\sigma \sim 0$)

$$F(M,X) \sim \frac{\sin^2(MX)}{\sin^2 X} \quad (2.7)$$

Then Eq. (2.4) can be written as

$$\frac{d^2 N}{d\Omega d\omega} = \frac{d^2 N_0}{d\Omega d\omega} 4\sin^2(\ell_2/Z_2) \frac{\sin^2(MX)}{\sin^2 X} \quad (2.8)$$

When the spacing between the foils ℓ_1 exceeds the formation length of the gap material Z_1 , $F(M,X)$ varies rapidly compared with the single-interface term given by Eq. (2.4) and the peak spectral intensity is found to vary as the square of the number of interfaces when $X = r\pi$ and r is an integer, neglecting photon absorption in the foils, variation in foil thickness and the multiple scattering. From Eq. (2.8) it is possible to determine the foil thicknesses that maximize photon production. This occurs for

$$X = r\pi, \quad (2.9)$$

and

$$\ell_2 Z_2 = (m - 1/2)\pi, \quad (2.10)$$

Where r and m are positive integers. Substituting these conditions into Eq. (2.8) gives

$$\frac{d^2 N}{d\Omega d\omega} = 4M^2 \left[\frac{d^2 N_0}{d\Omega d\omega} \right]. \quad (2.11)$$

Eqs. (2.9) and (2.10) are the coherence conditions, *i.e.*, the requirements for in-phase addition of the radiation from all interfaces. To minimize photon absorption and electron scattering, ℓ_1 and ℓ_2 should be as small as possible which means choosing $r = m = 1$, for these values.

$$\ell_{1,2} = (\pi/2)Z_{1,2}. \quad (2.12)$$

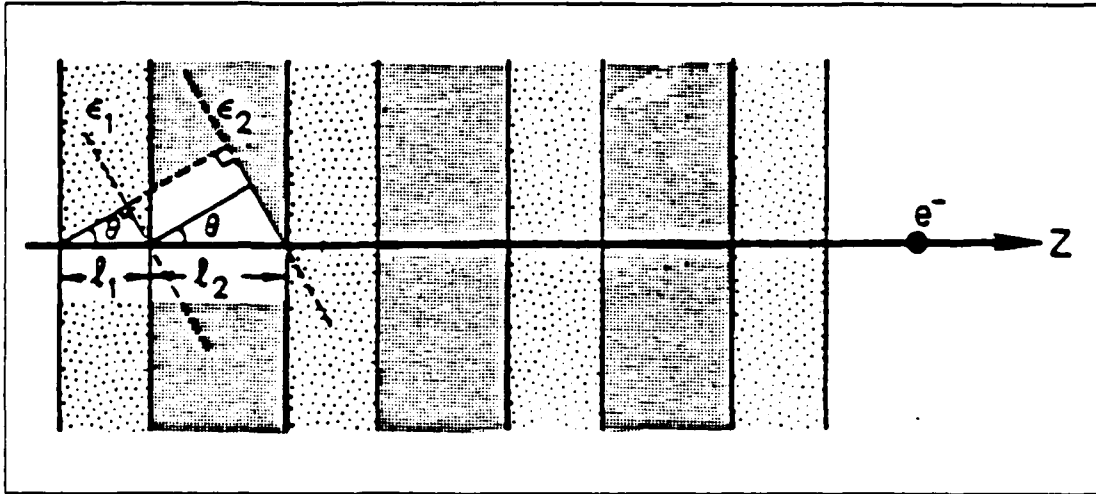


Figure 2.2 Condition for Coherent Phase Summation.

With the assumption that $\epsilon_{1,2} \sim 1$, from Eqs. (2.1) and (2.9) it is found that the angle for which resonance is satisfied is given by [Ref. 6: pp.264-275].

$$\cos\theta \sim \frac{\ell_1 + \ell_2}{\ell_1 \sqrt{\epsilon_1} + \ell_2 \sqrt{\epsilon_2}} \left[1 - \beta - \frac{2\pi r c}{\omega(\ell_1 + \ell_2)} \right]. \quad (2.13)$$

The in-phase radiation adds coherently and the resonance transition radiation is shown diagrammatically in Fig. (2.2).

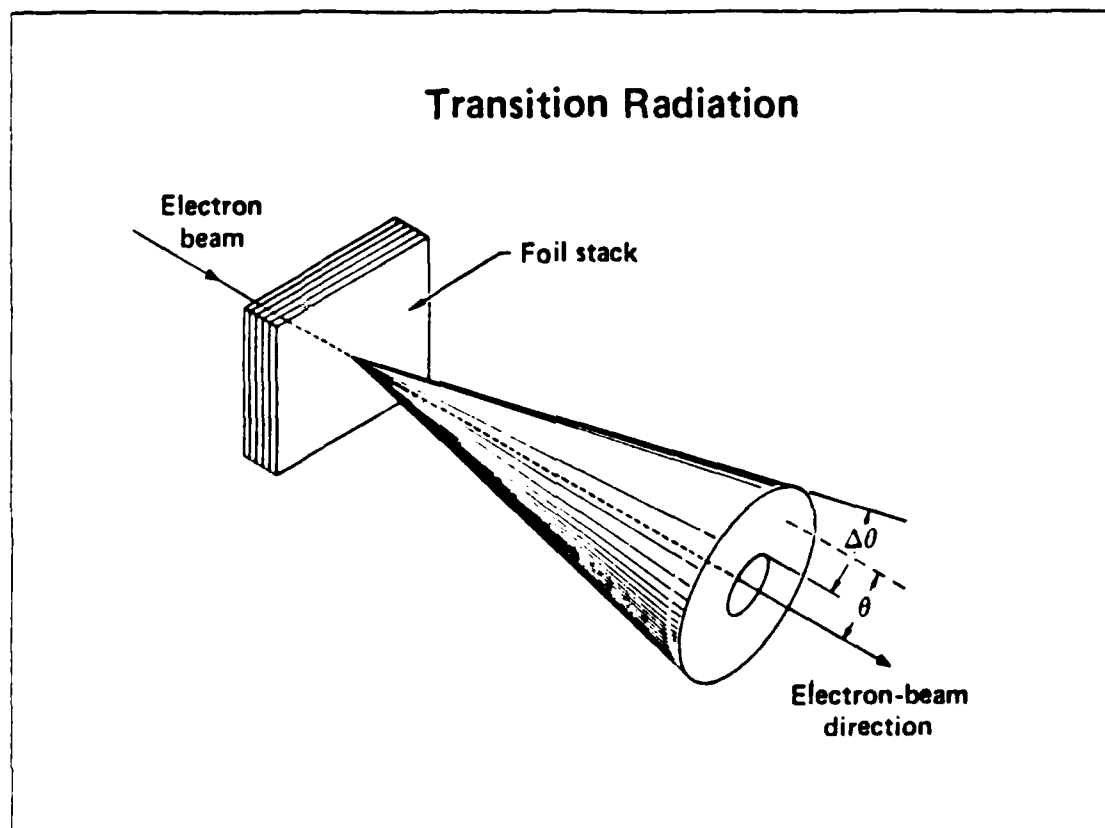


Figure 2.3 Schematic Diagram of the Transition Radiation Cone.

B. TRANSITION RADIATION CONE

Fig. (2.3) shows the transition radiation emitted in a tight forward direction. There is also an apex angle that maximizes the radiation $d^2N_0/d\Omega d\omega$ from a single interface. For the conditions $\theta^2 \ll 1$, $\epsilon_{1,2} \sim 1$, and $\beta \sim 1$, this optimizing angle can be derived from Eq. (2.13) [Ref. 4: p.1290]

$$\theta_{\text{opt}}^2 = 1/3\{-(\delta_1 + \delta_2) + [(\delta_1 + \delta_2)^2 + 12\delta_1\delta_2]^{1/2}\}, \quad (2.14)$$

where $\delta_i = [(1/\gamma)^2 + (\omega_i/\omega)^2]/2$ ($i=1,2$). If both Eq. (2.1) and Eq. (2.13) are satisfied for $\theta = \theta_{opt}$, the $d^2N/d\Omega d\omega$ is optimized. In general, $\omega_2 \gg \omega_1$, where ω_1 is the plasma frequency of the medium in which the foils are immersed. For the case of a foil stack in vacuum, $\omega_1 \sim 0$ and θ_{opt} reduces to

$$\theta_{opt} \sim 1/\gamma. \quad (2.15)$$

As the electron energy increases, the cone apex angle becomes small. This gives a highly directional and intensive forward beam.

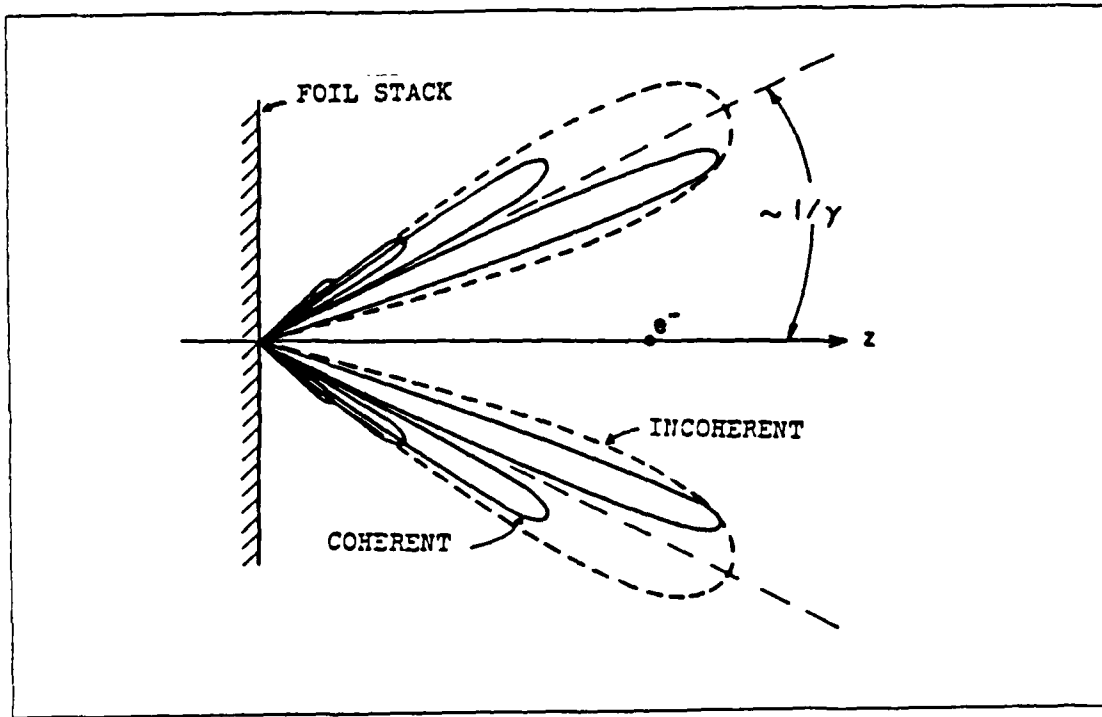


Figure 2.4 Coherent and Incoherent Transition Radiation from a Foil Stack.

For incoherent emission the photons can be separated from the emitting charged particle. For coherent radiation where there is inter-foil phase addition of the radiation, the lobe pattern will be broken into smaller lobes due to interfoil coherent addition of soft x-rays [Fig. (2.4)].

C. COMPUTER SPECTRUM ANALYSIS

By taking the approximate multi-foil absorption [Eq. (2.6)], the analytic expression for the transition radiation [Eq. (2.4)] can be written as

$$\frac{d^2N}{d\Omega d\omega} \sim 4 \left[\frac{d^2N_0}{d\Omega d\omega} \right] \sin^2(\ell_2/Z_2) \left[\frac{1 - \exp(-M\sigma)}{\sigma} \right] . \quad (2.16)$$

This expression was used for the differential production efficiency in spectrum analysis below. The analytic expression can be analyzed by dividing it into the three parts:

1. *The single interface intensity* $4d^2N_0/d\Omega d\omega$ [Eq. (2.3)]
2. *The single foil interference dependence* $\sin^2(\ell_2/Z_2)$ [Eq. (2.4)]
3. *The multi-foil interference dependence* $F(M, X)$ [Eqs. (2.5) and (2.6)]

1. Formation Length

The key to understanding the dependence of the three main terms on the photon energy and the stack variables is understanding the dependence of the formation length [Eq. (2.1)] on the photon energy and stack variables. The dependence of the transition radiation intensity on the formation length can be divided into three parts.

- a. *The single interface intensity depends on* $(Z_1 - Z_2)^2$
- b. *The single foil interference depends on the phase* (ℓ_2/Z_2)
- c. *The multi-foil interference depends on the phase* $(\ell_1/Z_1 + \ell_2/Z_2)$

The formation length Z_1 is inversely proportional to the photon energy [Fig. (2.5)]. The formation length Z_2 of the foil has the maximum value Z_{\max} at E_{critical} (critical energy of transition radiation above which the intensity becomes negligible). E_{critical} can be found by taking the first derivative of formation length Z_2 [Eq. (2.2)]

$$E_{\text{critical}} \sim \left(\frac{\gamma^2}{1 + \gamma^2 \theta^2} \right)^{1/2} E_2 . \quad (2.17)$$

where E_2 is the energy corresponding to the plasma frequency of dielectric foil. For $\theta = 1/\gamma$ at θ_{opt} Eq. (2.17) becomes $(\gamma/\sqrt{2})E_2$. Z_{\max} can be found by substituting Eq. (2.17) into Eq. (2.2)

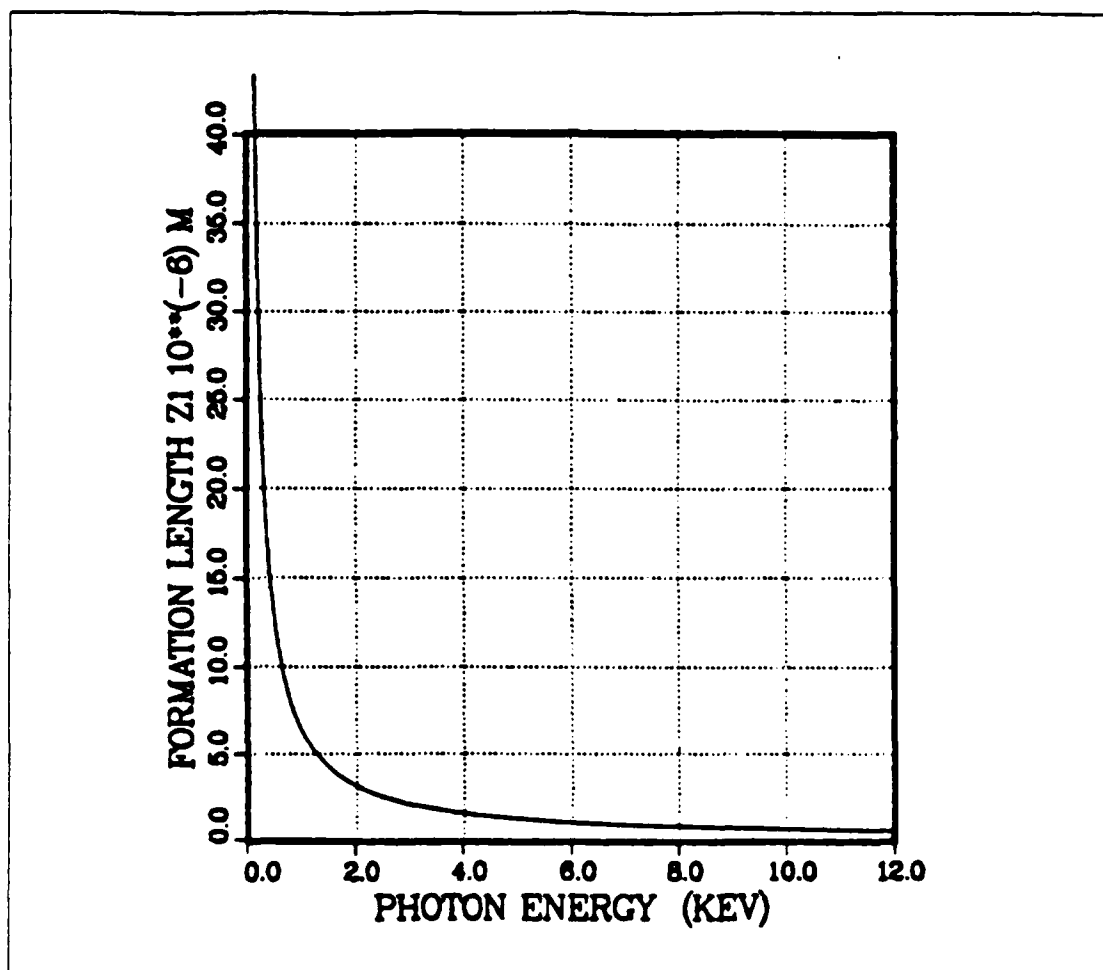


Figure 2.5 Formation Length of Vacuum ($E_1 = 0$, $\gamma = 127$, $\theta \sim 1. \gamma$).

$$Z_{\max} = \frac{2hc}{E_2 \sqrt{1. \gamma^2 + \theta^2}} \quad (2.18)$$

for $\theta = 1. \gamma$ at θ_{opt} then $Z_{\max} = (\sqrt{2} E_2) hc \gamma$. For photon energies $E \ll E_{\text{critical}}$ the formation length of the dielectric becomes independent of γ and is inversely proportional to the square of the medium plasma energy

$$Z_2 = 4hc(E. E_2^2) . \quad (2.19)$$

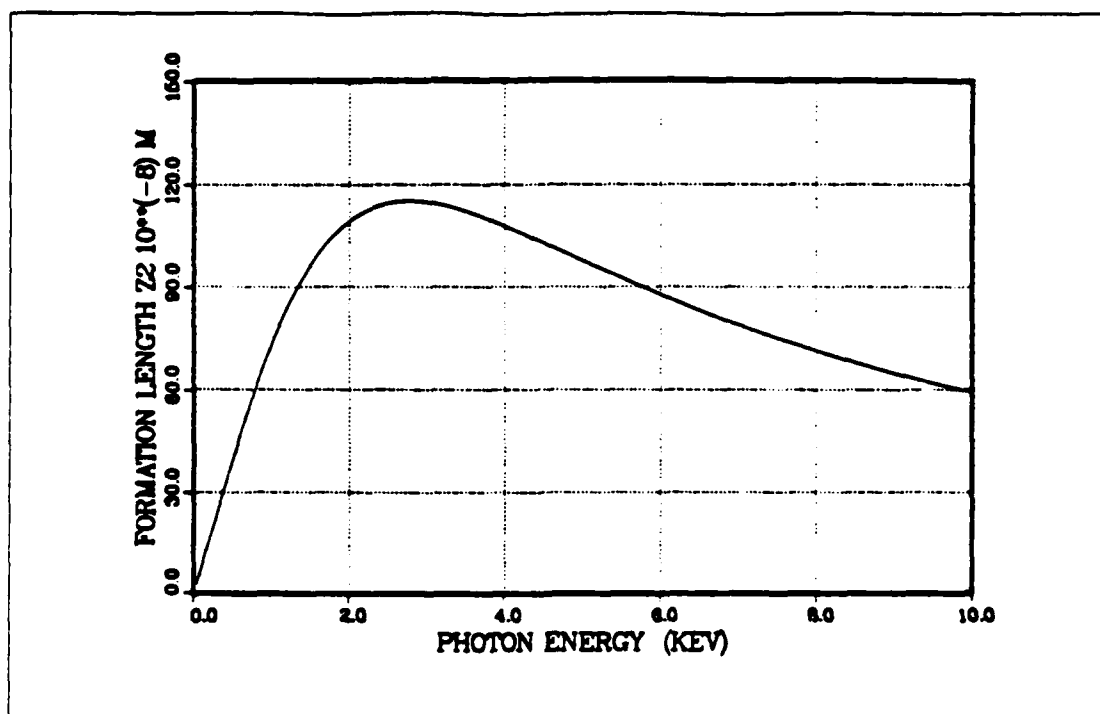


Figure 2.6 Formation Length of Al ($E_2 = 32.8 \text{ eV}$, $\gamma = 127.0 \sim 1 \gamma$).

At the critical energy the formation lengths Z_1 , Z_2 are approximately equal, and the single interface intensity becomes small. Therefore, above the critical energy the transition radiation intensity will be negligible. Figs. (2.6) and (2.7) show the dependence of the formation length of Al and Mylar on photon energy for $\theta_{\text{opt}} \sim 1 \gamma$ and $\gamma = 127$. For photon energies below the critical energy (2.95 keV, 1.79 keV for Al and Mylar) the formation length is approximately linear with energy and independent of γ . The formation length Z_2 of Mylar is longer than Al and Mylar has lower critical energy than Al because of the smaller plasma frequency.

2. Single Interface Intensity

The single interface intensity $d^2 N_{\omega} d\Omega d\omega$ [Eq. (2.3)] limits the spectrum to the maximum photon energy approximately equal to $\gamma E_2 \sqrt{2}$ for a vacuum dielectric stack. Above this energy, the spectrum is proportional to $1/\omega^4$. Figs. (2.8) and (2.9) show that $d^2 N_{\omega} d\Omega d\omega$ falls off more quickly for a Mylar vacuum interface than for a Al vacuum interface. The single interface intensity is also the factor which limits emission of transition radiation to a small forward angle approximately equal to 1γ .

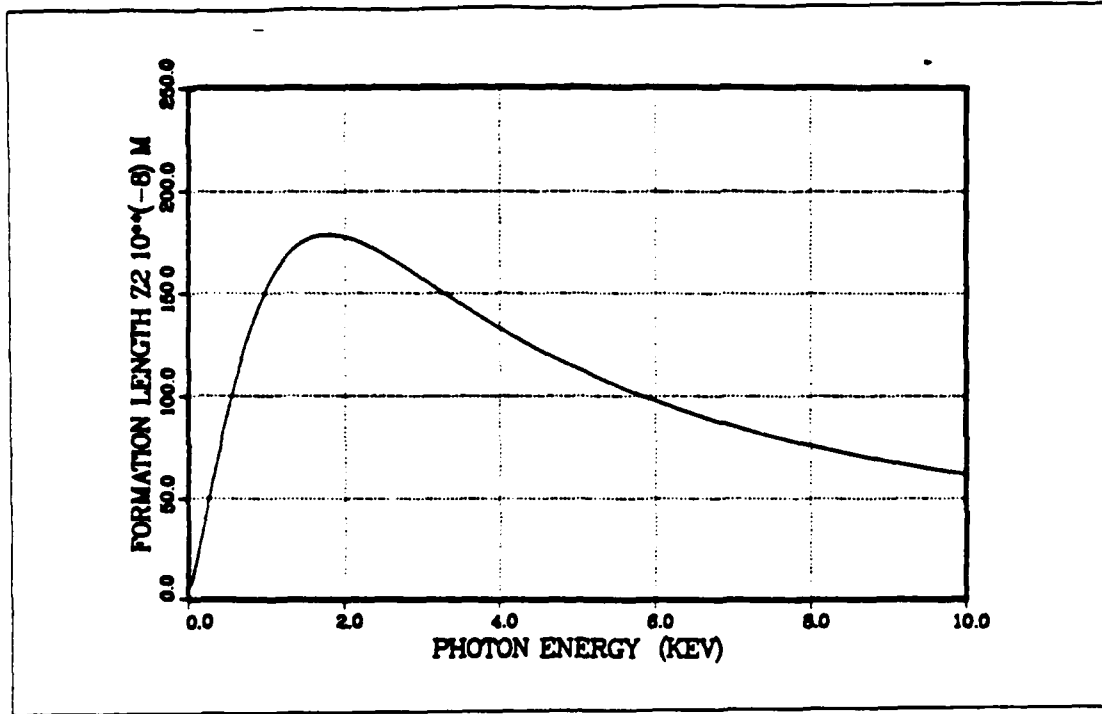


Figure 2.7 Formation Length of Mylar ($E_2 = 19.9$ eV, $\gamma = 127$, $\theta \sim 1 \gamma$).

3. Single Foil Interference Factor

The single foil interference term $\sin^2(\ell_2 Z_2)$ is an important factor in the resonance condition. Single foil resonance condition occurs at the photon energy E_m satisfying the condition Eq. (2.10) $\ell_2 = Z_2 (2m-1)\pi/2$ with m an integer. The phase slippage of the particle during transit through the foil is $(2m-1)\pi/2$, and the radiation of opposite phase produced at each interface as the particle enters and exits the foil interferes constructively. The phase slippage accounts for coherent addition of amplitudes from the two interface of a single foil and gives a peak value twice as large as from two interface when the emission is completely random. Figs. (2.10) and (2.11) show single foil interference factors of Al and Mylar with respect to photon energy. Mylar has a longer formation length Z_2 than Al [Figs. (2.6) and (2.7)] and 2.5 times bigger foil thickness than Al. The Mylar has a second peak at a smaller photon energy than Al. Fig. (2.12) shows the single foil interference factor as a function of photon energy for different foil thickness. The photon energies corresponding to the single foil resonance can be found from the first peak curves.

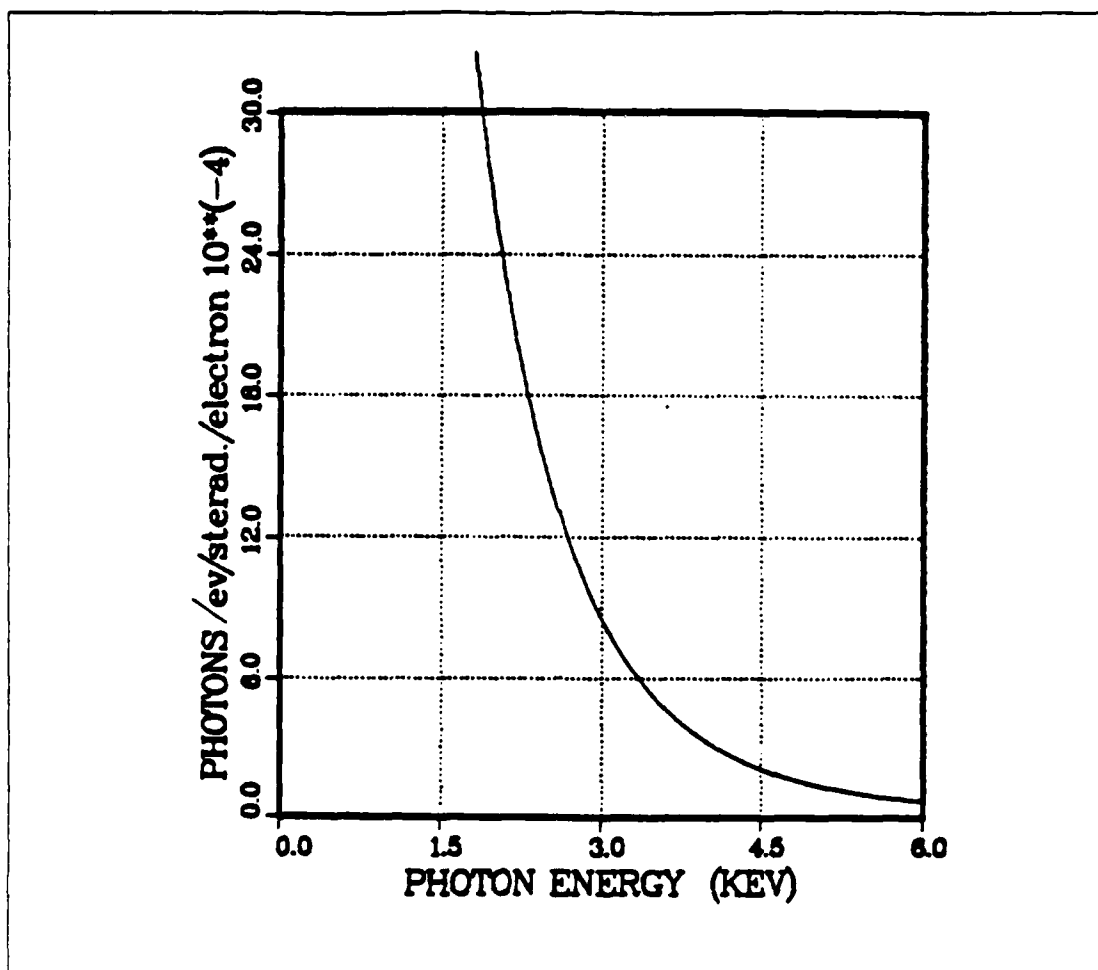


Figure 2.8 Single Interface Factor of Al ($\gamma = 127$).

4. Multi-foil Interference Factor

The multi-foil interference factor $F(M,Z)$ [Eq. (2.5)] results from the same interference phenomena as for the single foil interference factor. It includes the effect of absorption of photons within the foil stack.

As the number of foils in a stack is increased, intensity at the fixed photon energy is increased up to the saturated value. Fig. (2.13) shows the multi-foil dependence according to the number of foils. The absorption factor approximately increases linearly with number of foils. When $M\sigma \gg 1$ the asymptotic value for $F(M,X)$ is $1/\sigma(\omega)$. After this value is attained, the radiation intensity can not be increased by increasing the number of foils. A approximate condition for foil

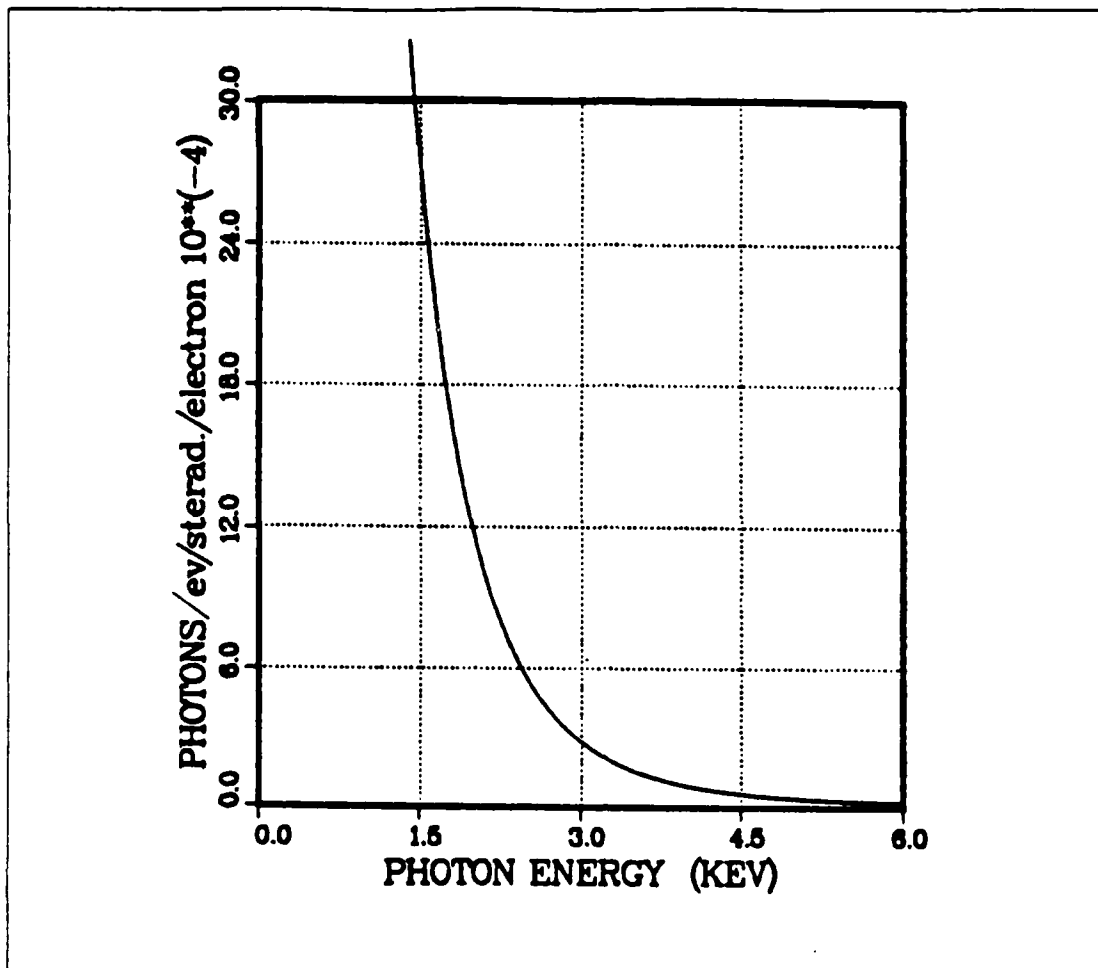


Figure 2.9 Single Interface Factor of Mylar ($\gamma = 127$).

saturation of transition radiation spectrum is $M\sigma \sim 1$. If the resonance condition is satisfied, then the radiation from successive foils interferes constructively, and $F(M,X) \sim M^2$ for negligible absorption (with M the number of foils). For $M \gg 1$, $F(M,X)$ can be approximated as a series of delta functions located at the resonance angles given by Eq. (2.13). Fig. (2.14) shows the photon energy dependence of $F(M,X)$ for Mylar / vacuum with the number of foil 8 and foil thickness $2.5\mu\text{m}$. In addition to absorption, particle scattering and random variation in foil thickness and spacing reduce the resonance effect. [Ref. 7]

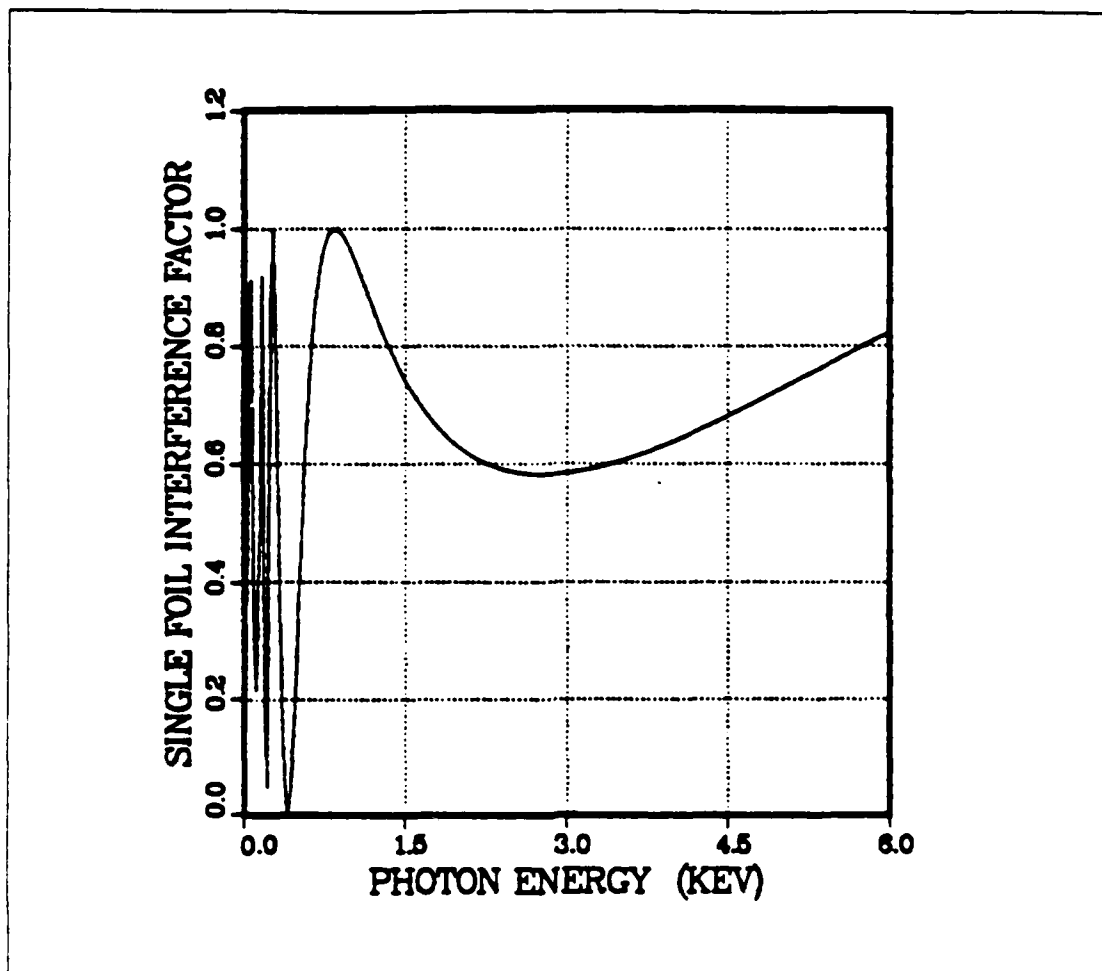


Figure 2.10 Single Foil Interference Factor of Al ($\ell_2 = 1\mu\text{m}$).

5. Shape of the Transition Radiation

The shape of spectrum [Eq. (2.16)] is determined by the three main characteristics:

- a *The absorption of the radiation in the foils*
- b *The critical photon energy $\hbar\omega_c = \gamma\hbar\omega_2$*
- c *The constructive interference between interfaces of single foil.*

The effect of these factors is shown for three cases. Where the transition radiation intensity is plotted as a function of energy for three cases : (1) for no absorption -- single interface factor [Figs. (2.8) and (2.9)], (2) for absorption but no single foil coherence -- single interface x multi-foil absorption factor [Fig. (2.15)], (3)

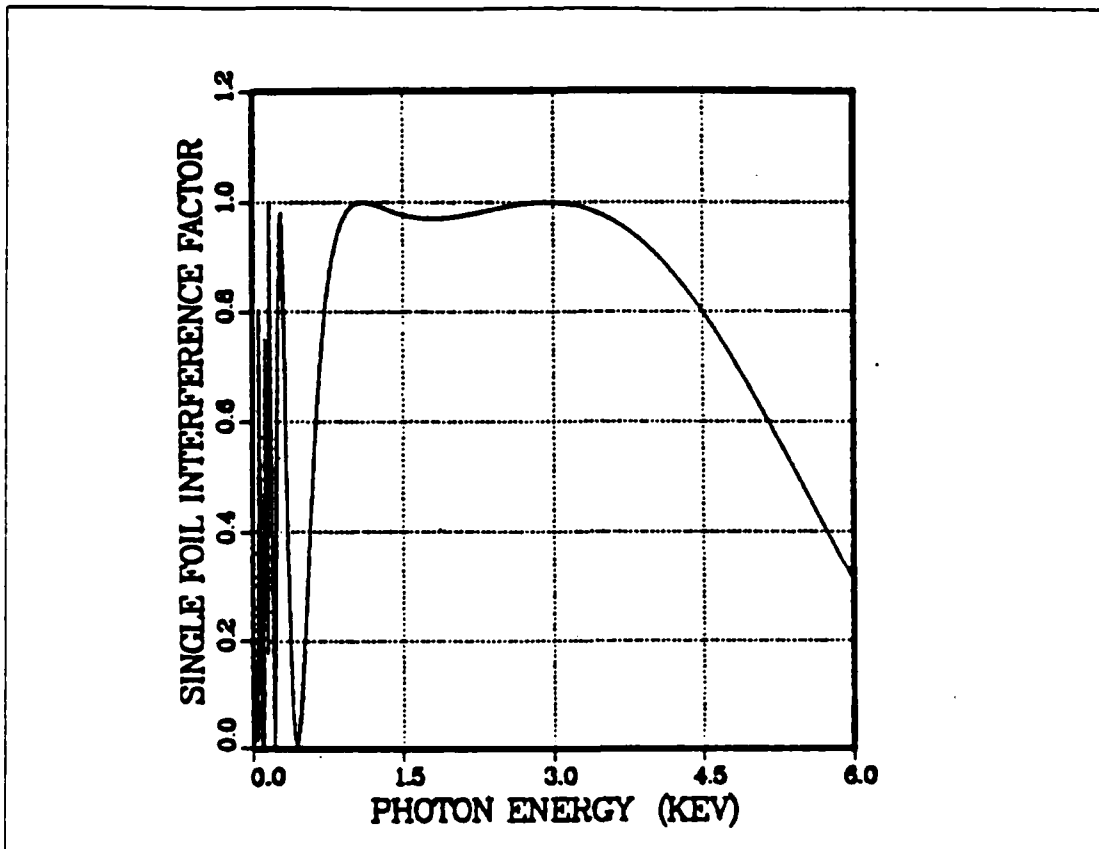


Figure 2.11 Single Foil Interference Factor of Mylar ($\ell_2 = 2.5\mu\text{m}$).

for both absorption and single foil coherence -- differential production efficiency [Figs. (2.16), (2.17), (2.18), and (2.19)].

When the losses due to the absorption in the foils are included, the reduction of the low-energy photons occurs and the drop-off at the high energy end of the spectrum is determined by the critical energy $\hbar\omega_c$. Above this energy the spectrum drops off as $(\omega_c/\omega)^4$.

The second term in Eq. (2.16) $\sin^2(\ell_2 Z_2)$ accounts for coherent addition of amplitudes from the two interfaces of the single foil and gives a peak value twice as large as from two interfaces when the emission is completely random. This occurs when there is constructive interference between the waves generated at the front and back interfaces [Ref. 8: pp.336-339]. The radiation intensity is maximized when the thickness of the foil is such that both the electron and the photon travel an integral number of wavelengths in the field generated at the first interface.

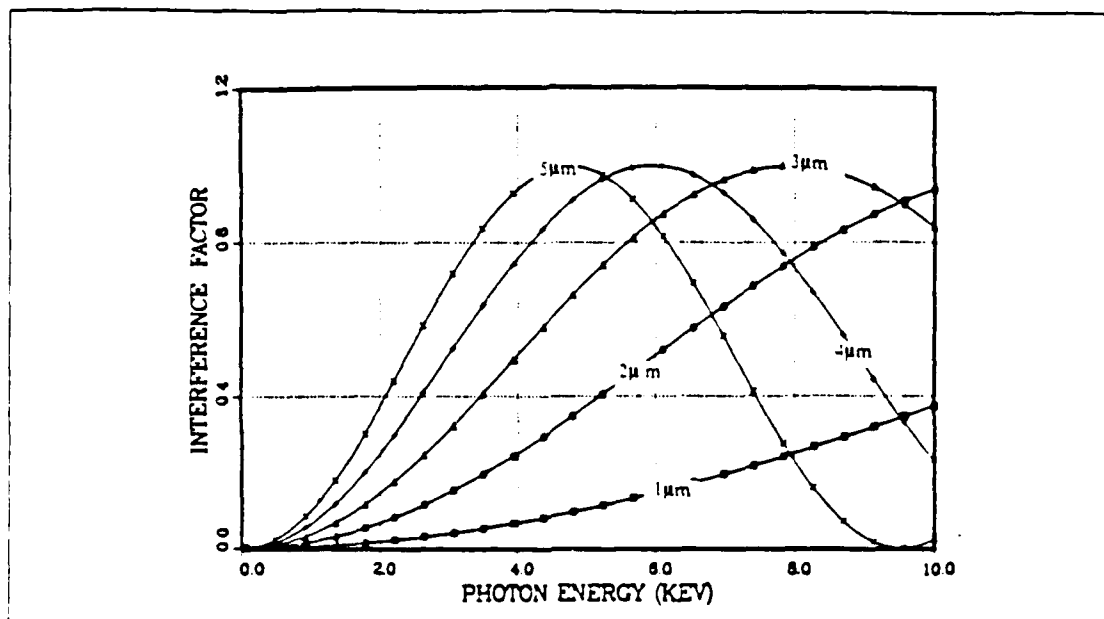


Figure 2.12. Single Foil Interference Dependence on Foil Thickness in Mylar ($E_2 = 19.9$ eV).

The spectral shape from a transition radiator is closely related to the thickness of the individual foil [Eqs. (2.4) and (2.5)] not only because the formation length [Eq. (2.1)] is needed for photon production but also because of absorption of the emitted radiation in the foils [Eq. (2.6)]. For low energy photons, absorption is of concern and can be minimized by making the foils as thin as possible; however if the thicknesses are made thinner than the formation length, photon production will also stop. Thus, the peak production intensity occurs at the photon energy corresponding to the formation length Z_2 equivalent to foil thickness [Ref. 9: p.3604]. There is an optimum foil thickness that balances production with re-absorption to give the maximum photon yield. This is shown in Fig. (2.20) for the case of Mylar 8 foils. The number of foils M is kept constant and the thickness is varied. The magnitude and peak emission can be predicted.

The spectral shape is influenced by not only an optimization procedure of minimizing absorption with thin foils but also by using as large a value of M as feasible. As the number of foils increases both scattering and photon absorption increase, thereby destroying coherence and ultimately preventing emission from photons. Neglecting multi-foil scattering, as the number of foils increases the peak

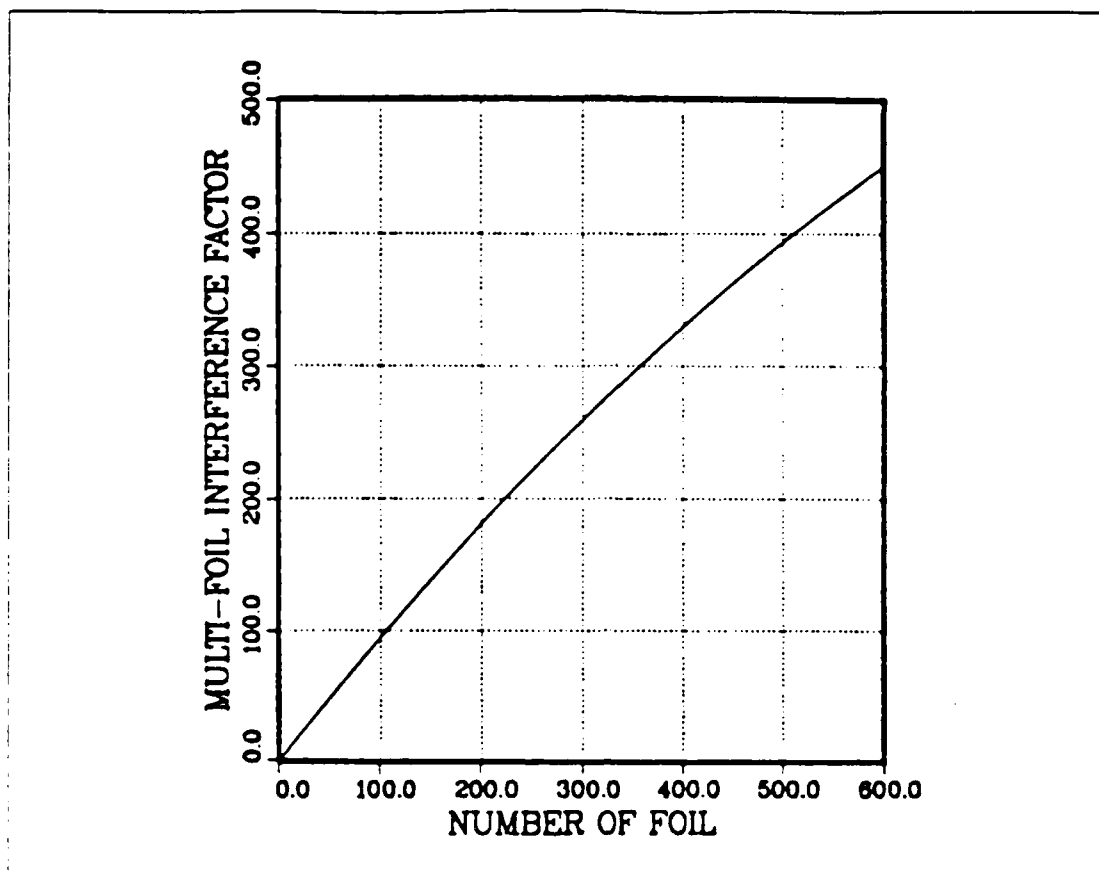


Figure 2.13 Effect of the Number of Foil on the Multi-foil Factor ($\sigma = 0.001$).

sharpens and increases in intensity as M^2 [Eq. (2.11)], however, since absorption also increases with M [Fig. (2.14)], a final value for photon production is reached where increasing M does not result in increased production. Fig. (2.21) shows a limiting effectiveness of increasing M , there is small gain in intensity after $M \sim 20$.

The increase in absorption above the K-edge results in a narrower energy spectrum than would otherwise be measured. Fig. (2.22) shows the calculated effect of K-shell absorption for Al on the radiation spectrum for 65 MeV electron beam energy with K-edge 1560 eV. As the absorption coefficient increases, the intensity decrease sharply. The narrow spectrum is due to the sudden change in x-ray absorption at the K photoabsorption edge in the material. The curve does not include the effect of the detector resolution.

The purpose of this experiment has been divided into three areas:

- (a) *The x-ray radiation is emitted in a forward cone with the apex angle of the*

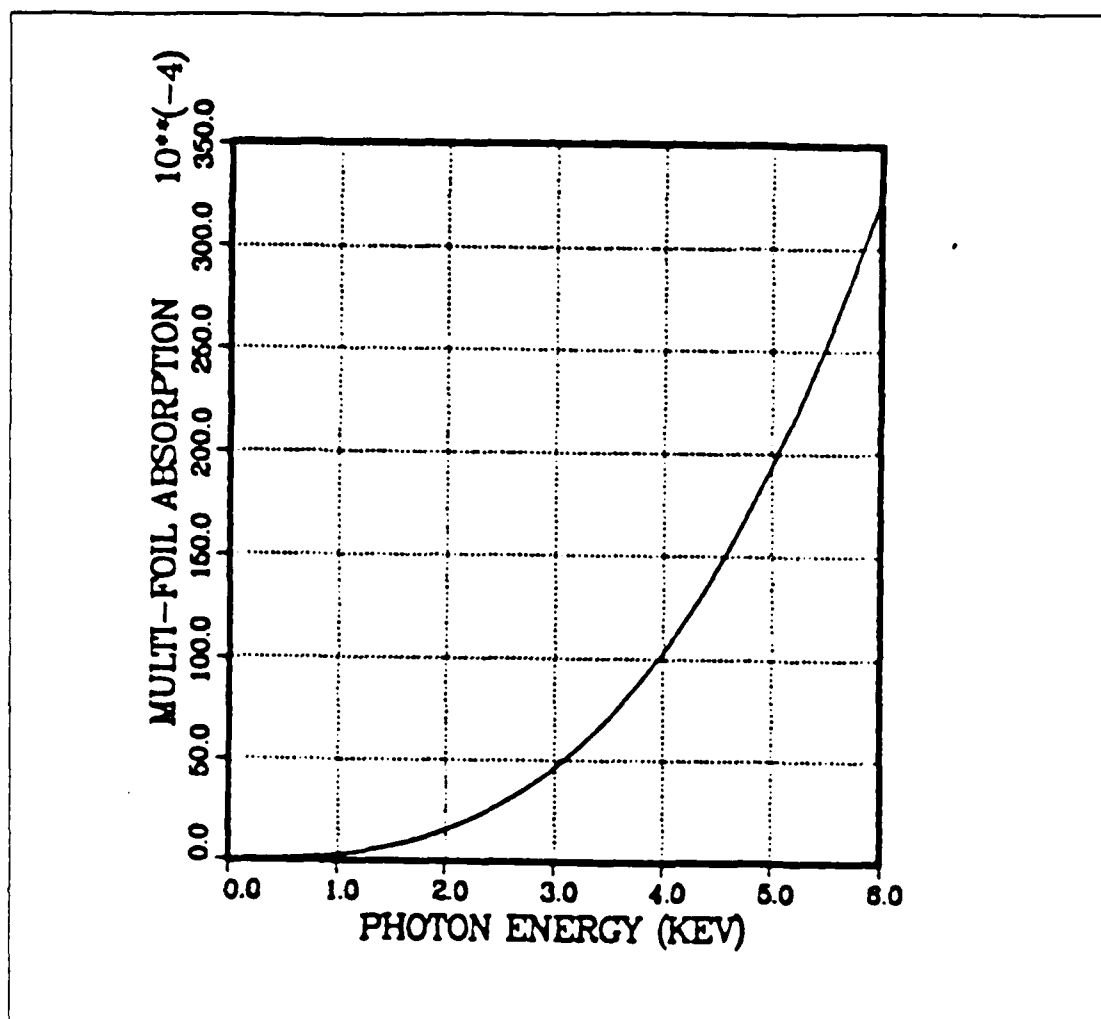


Figure 2.14 Multi-foil Absorption Factor of Mylar ($M = 8$, $\ell_2 = 2.5\mu\text{m}$).

cone at approximately 1.7° . The measurement of the apex angle was done by improvements in collecting data using a motor-driven detector.

- (b) The absolute differential production efficiencies for soft x-rays emitted from radiator were compared with the theoretical predictions and interpreted in terms of absorption and coherence by measuring the peak and FWHM bandwidth energy (full width of the spectrum between points having half the maximum production efficiency).
- (c) The narrower frequency spectrum was predicted by the increase in absorption above the K edge, and the effect of the K edge was compared with no K-shell absorption edge.

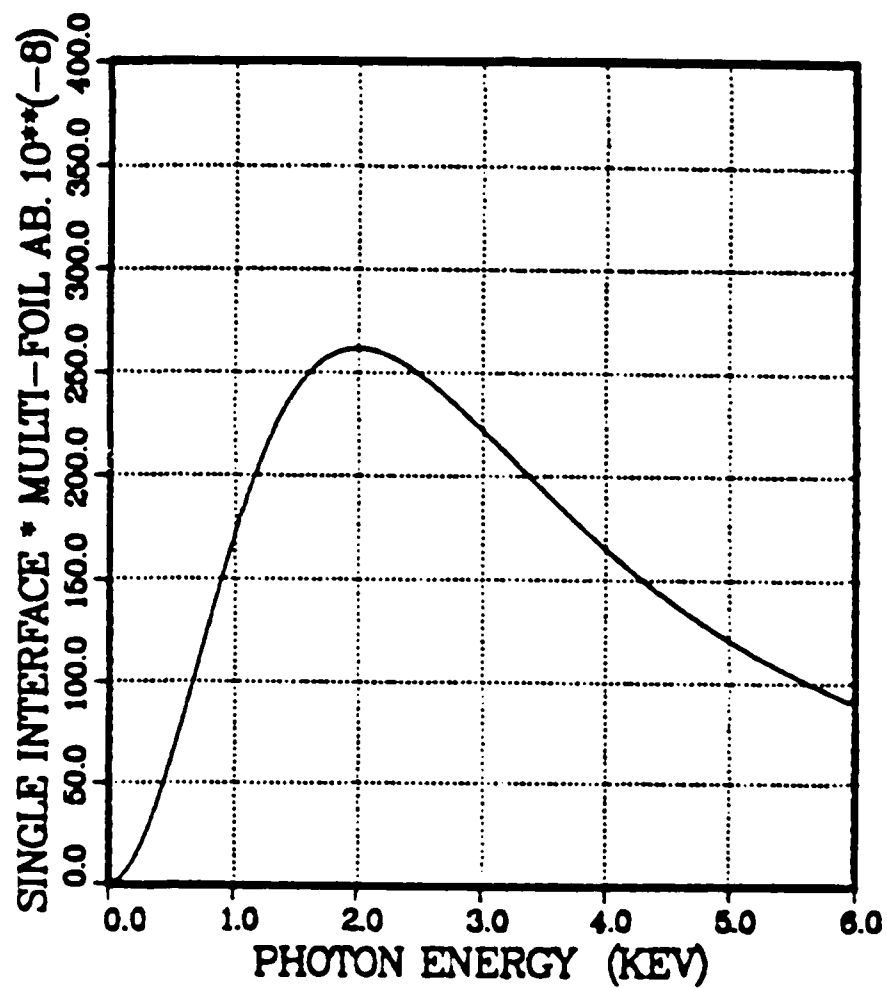


Figure 2.15 Absorption Factor of Mylar (Single Interface x Multi-foil Absorption).

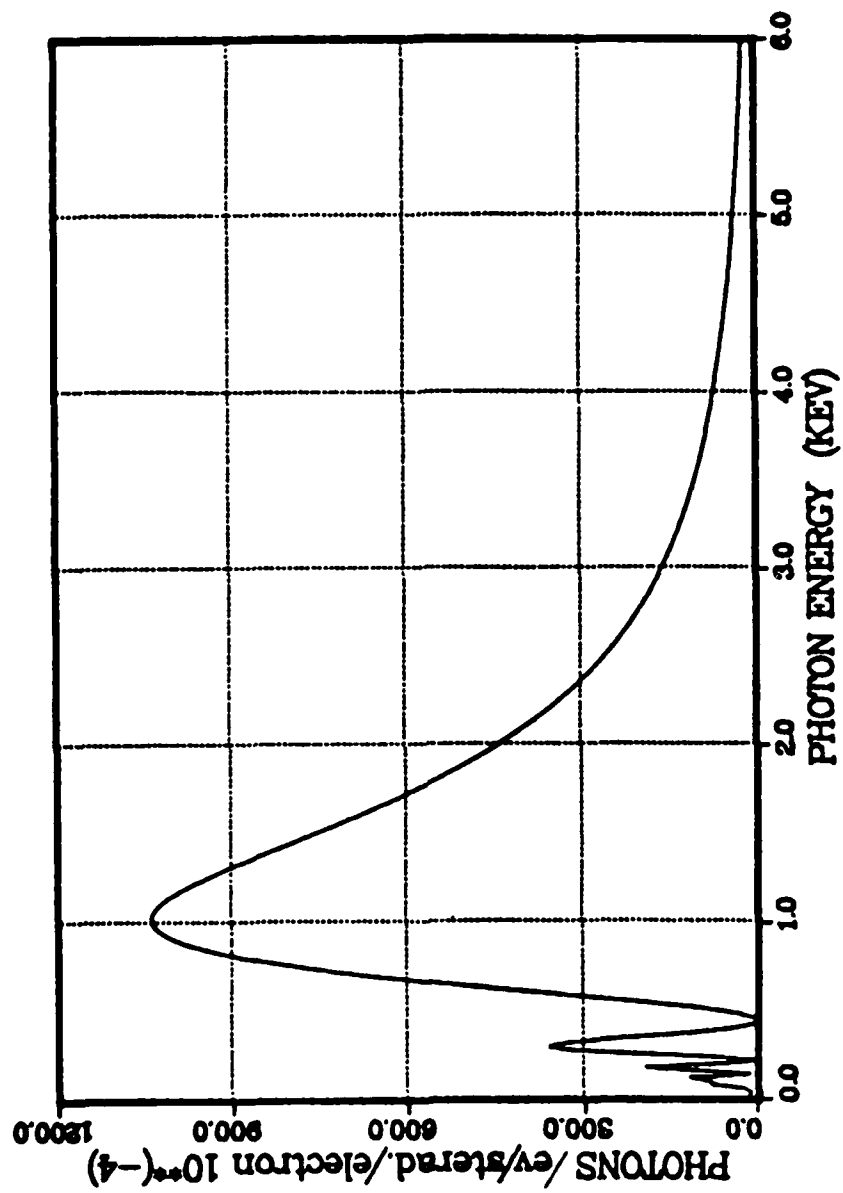


Figure 2.16 Calculated Differential Production Efficiency
from 30 Foils 1 μ m Al.

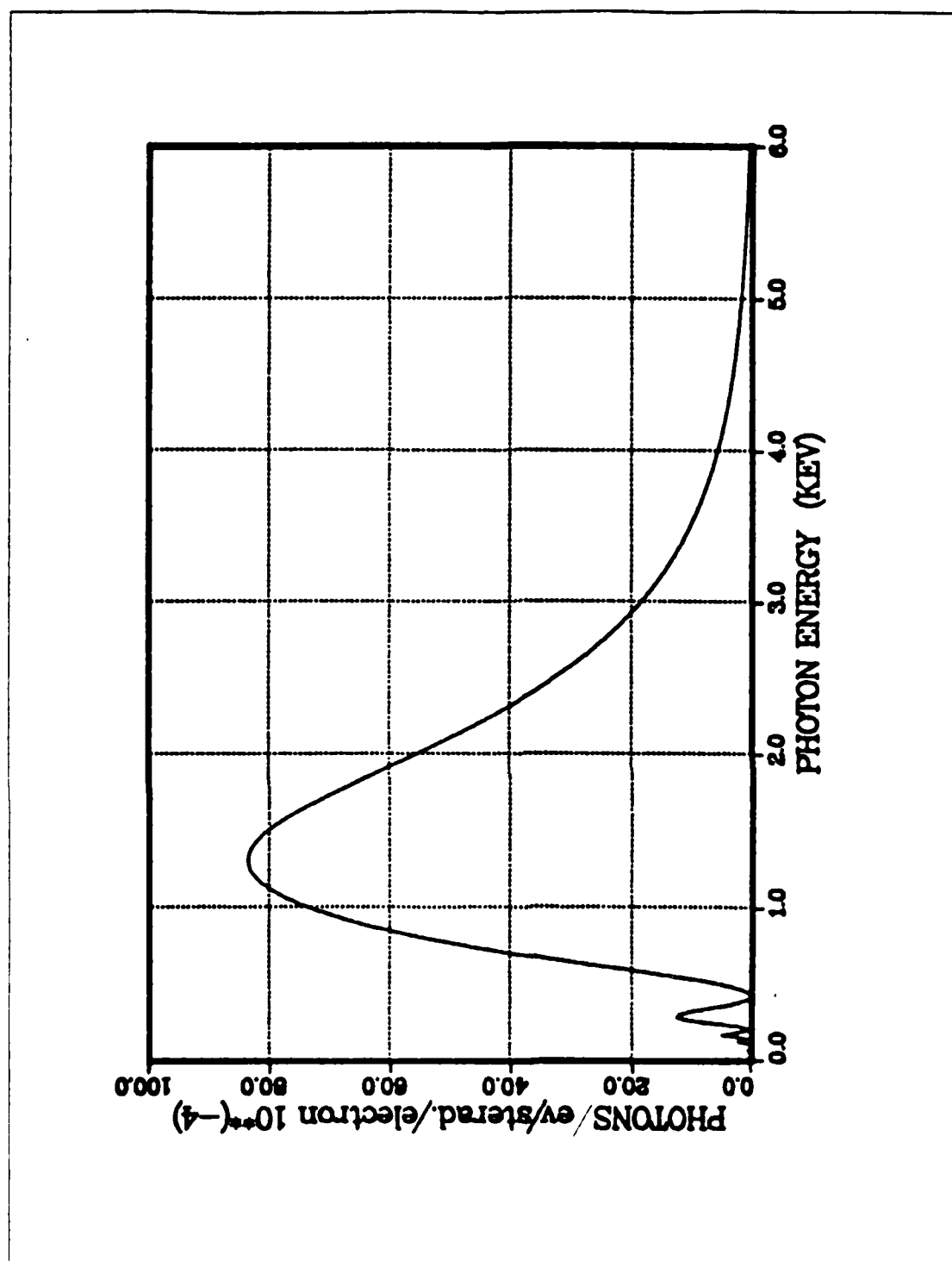


Figure 2.17 Calculated Differential Production Efficiency
from 8 Foils 2.5 μ m Mylar.

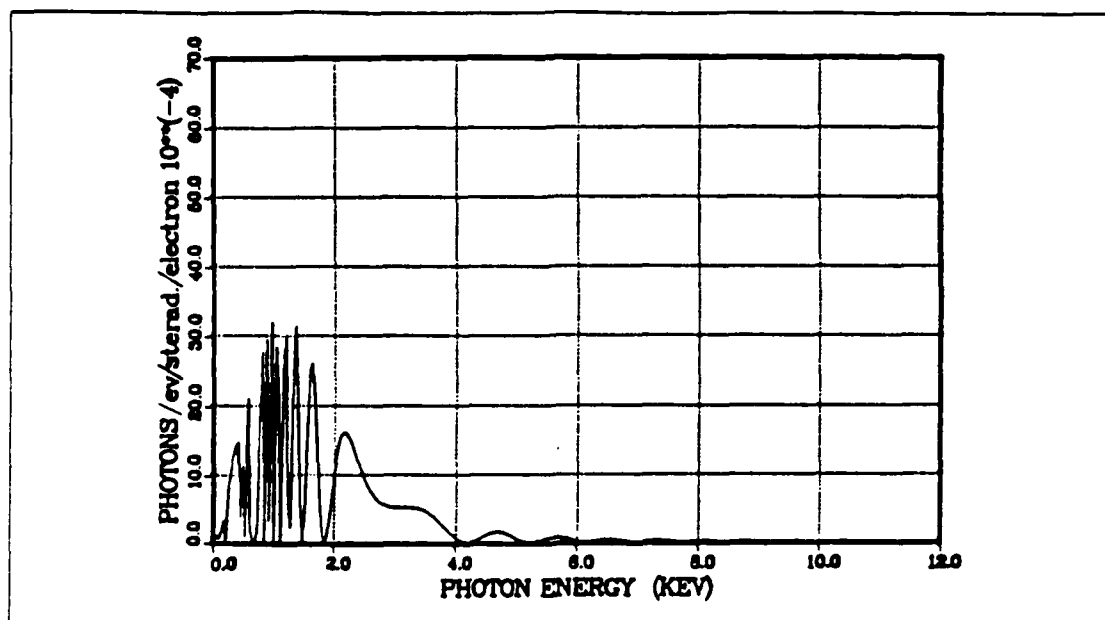


Figure 2.18 Calculated Differential Production Efficiency
from 1 Foil 26 μ m Al.

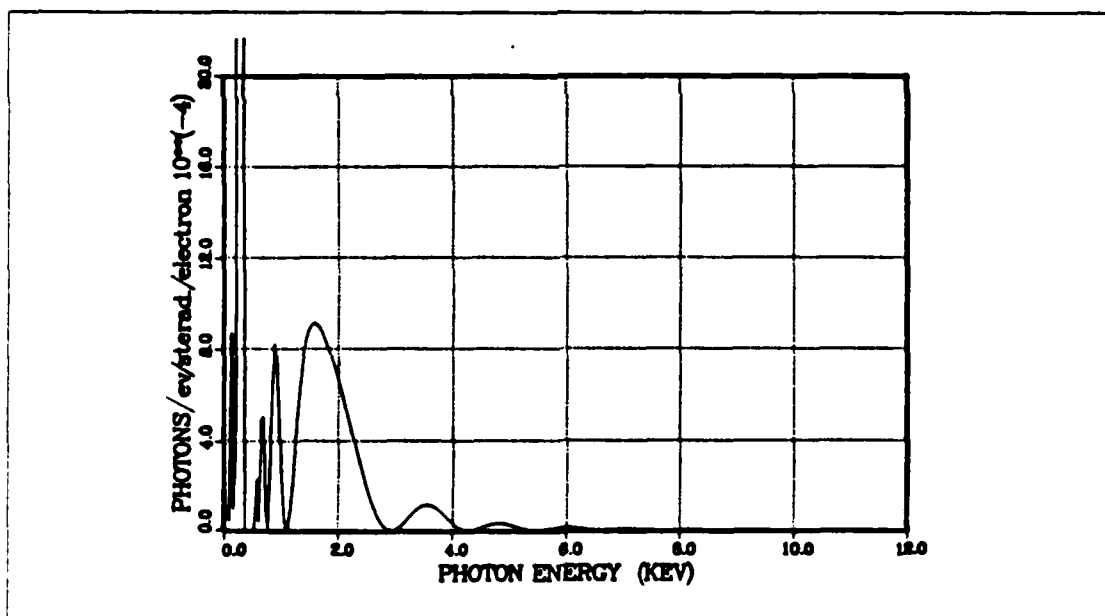


Figure 2.19 Calculated Differential Production Efficiency
from 1 Foil 19 μ m Mylar.

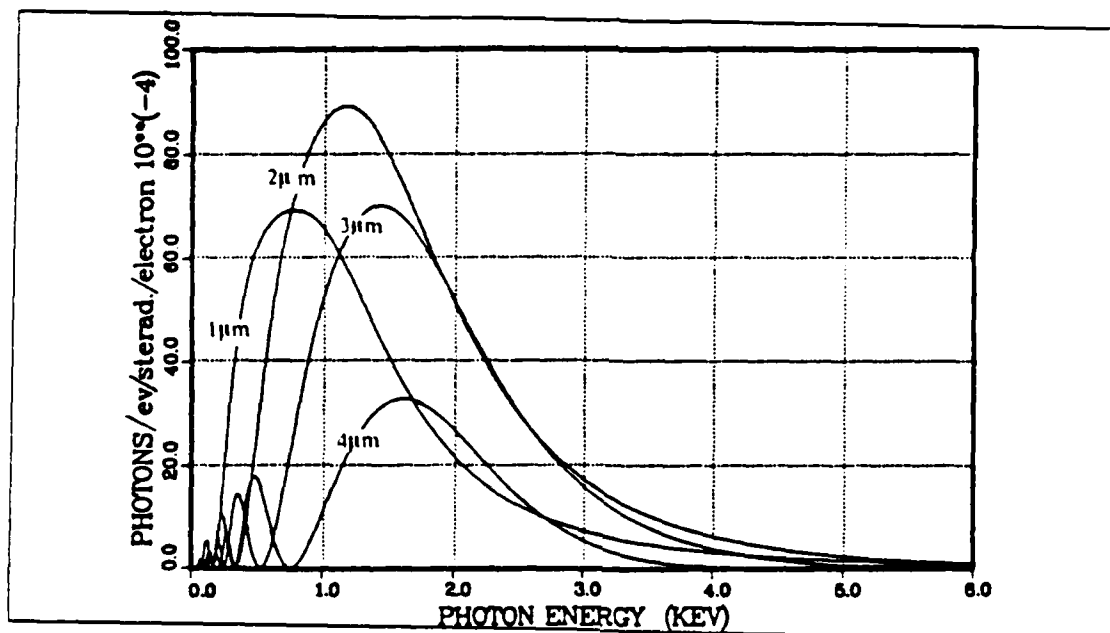


Figure 2.20 Calculated Spectral Distribution from 8 Foils of Various Thickness of Mylar for 65 MeV.

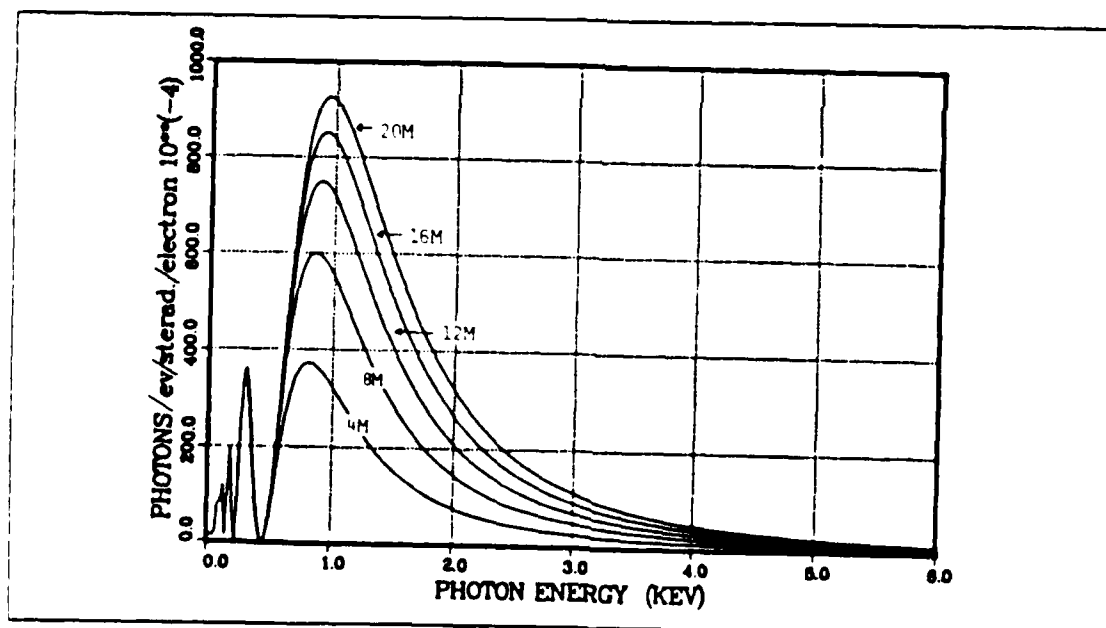


Figure 2.21 Effect of the Number of Foils on the Radiation Peak of the $1\mu\text{m}$ Al.

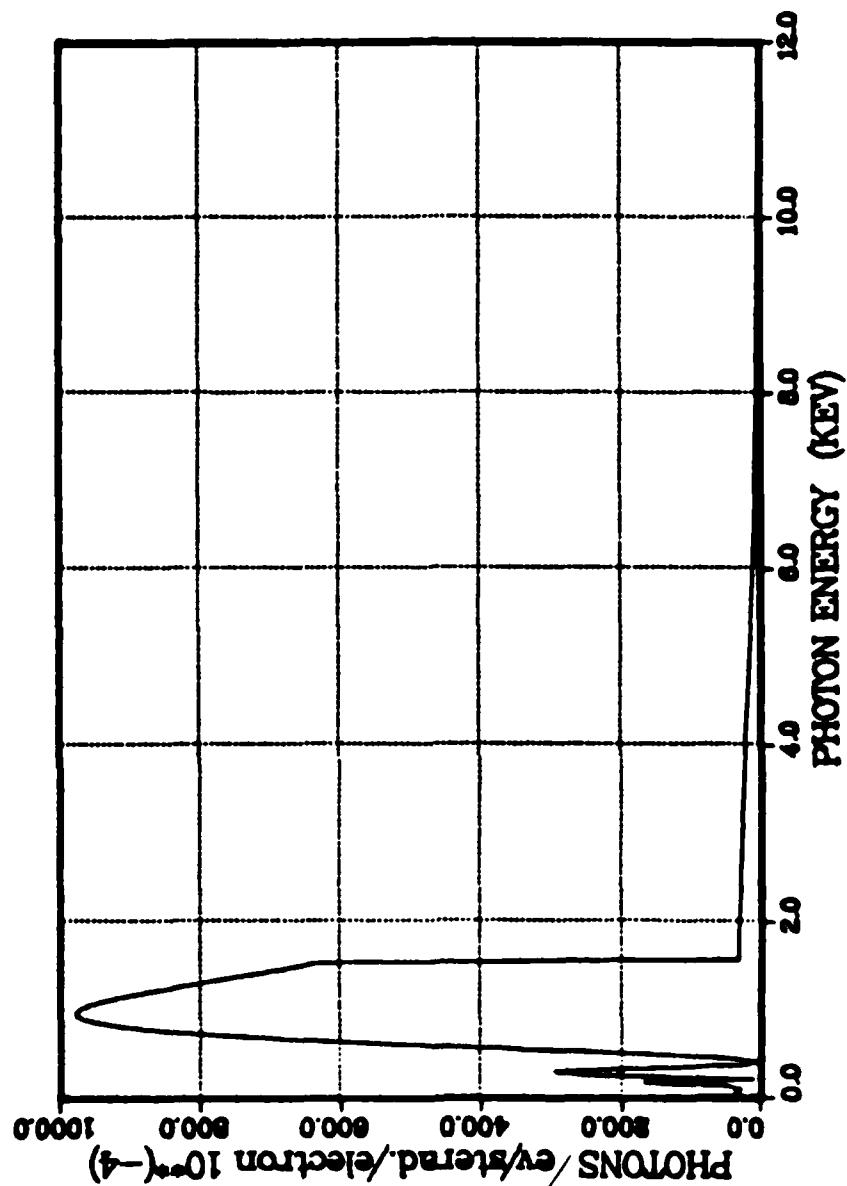


Figure 2.22 Calculated Effect of K-shell Absorption on the Al Spectrum for 65 MeV Electron.

III. EXPERIMENTAL APPARATUS

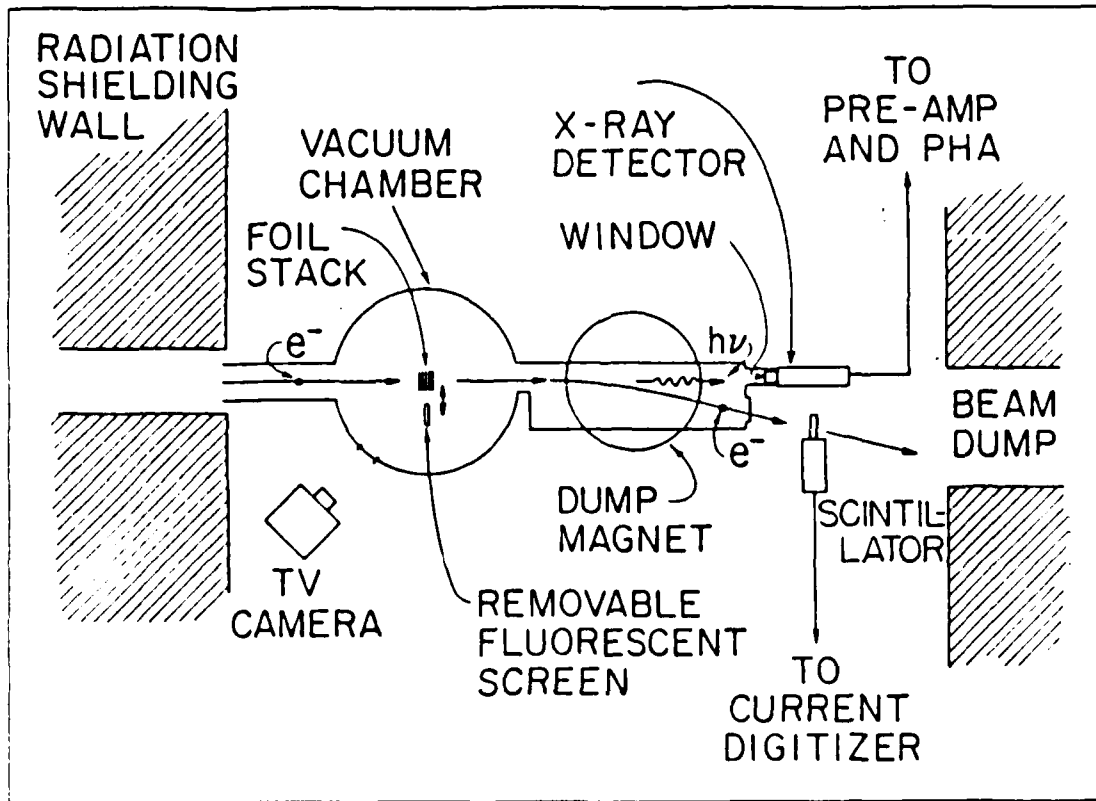


Figure 3.1 Schematic Diagram of a Experimental Apparatus.

A. EXPERIMENTAL CONCEPT

The experiment was done at the Naval Postgraduate School at Monterey California using a medium energy linac. The experimental apparatus is shown in Fig. (3.1). Electrons enter from the left-hand side into a vacuum chamber where they pass through the foil stacks, and then through the dump magnet to be deflected out of the path of photon detector. During their passage, the x-rays travel entirely in a 10^{-6} Torr vacuum penetrating the 1000 Å window of the proportional counter. Throughout the run, the transition radiation photons were detected with a gas-flow x-ray proportional counter. Five foil stacks were mounted on a movable platform holder so that five

different targets can be used without changing the vacuum. A phosphor (ZnS) target was used for the alignment of the electron beam relative to the target chamber. The detector was periodically calibrated using a Fe^{55} source. The current pulse height was monitored using a scintillator just before the beam dump. In this manner the total charge was kept constant for each measurement.

B. EQUIPMENT PERFORMANCE

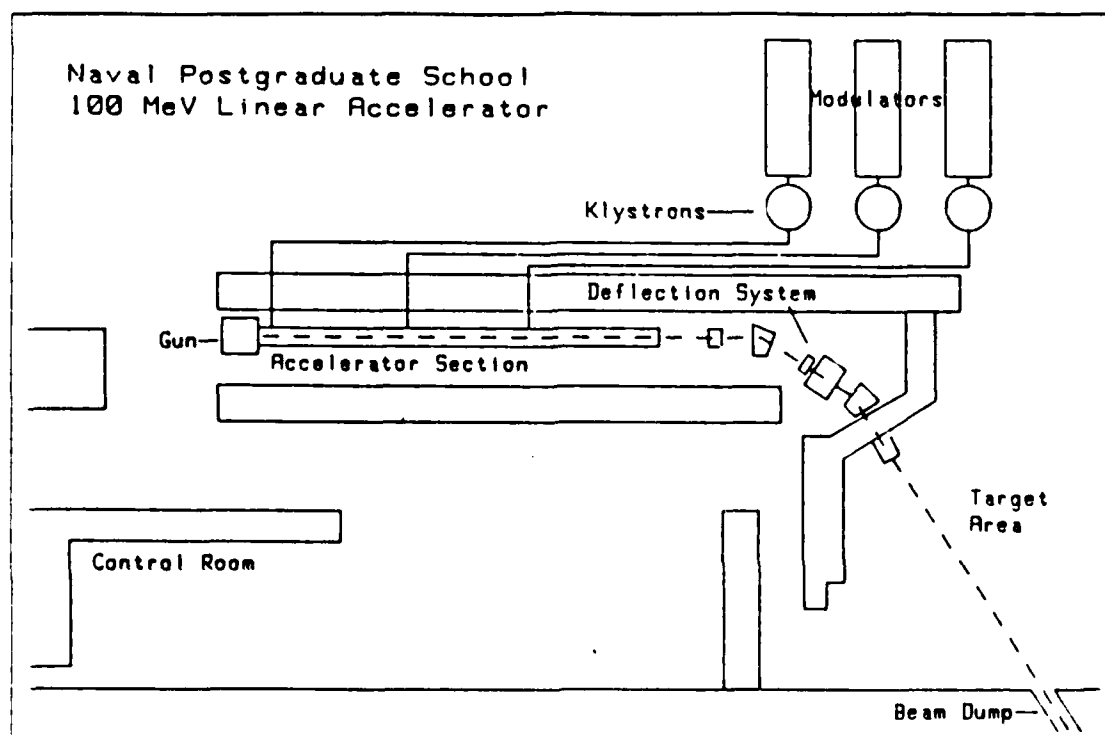


Figure 3.2 Schematic Diagram of a Linear Accelerator.

1. Linac

The linear accelerator (Linac) is used to produce high-energy electron bunches [Fig. (3.2)]. As for general characteristics, the linac is similar to the Stanford linear accelerator Mark 3, which has 1000 MeV kinetic electron energy, while the NPS linac is 9.14 m long and 100 MeV. An electron gun at the beginning of the accelerator injects electrons at roughly $\beta = 0.5$. The design of the accelerator sections causes the energy to propagate in the TM mode. The injected electrons are accelerated to near the velocity of light in their first few centimeters of travel. Coupled klystrons produce

a travelling TM mode wave along the wave guide. The electron speed and the wave speed are about the same, so that the electric field of the wave will accelerate the electrons. Thus, the electrons gain energy at the expense of the wave.

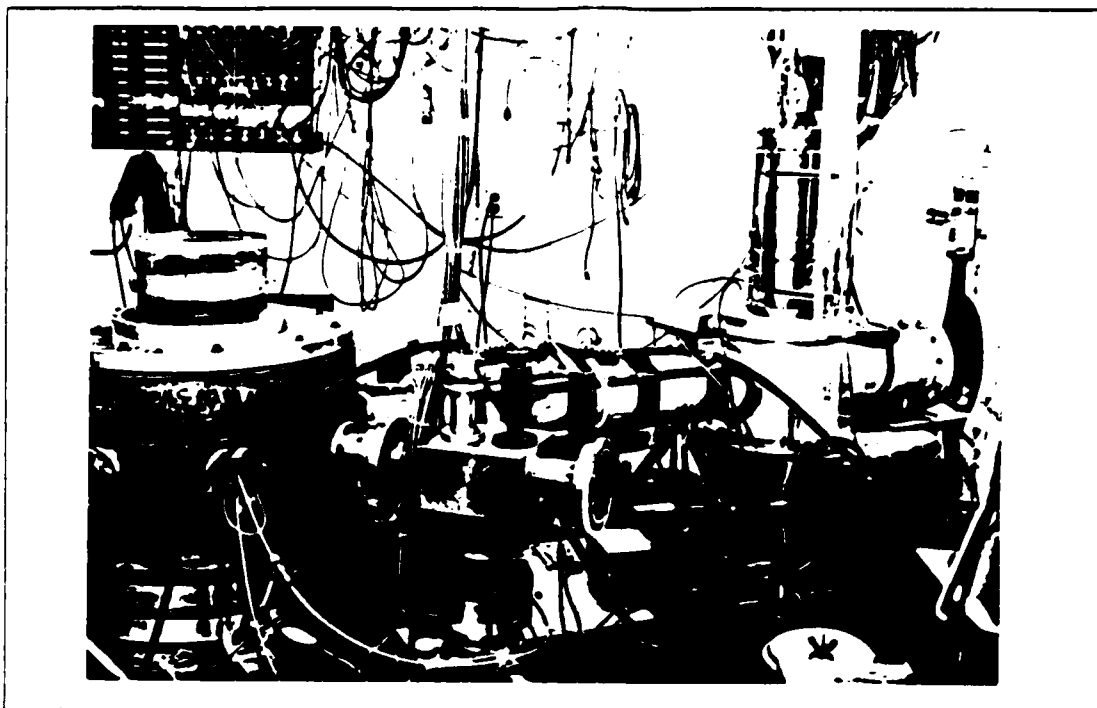


Figure 3.3 Target and Detector Chamber.

2. Target and Detector Chamber

The target and detector chamber are made of aluminum and the picture is shown in Fig. (3.3). During the experiment the whole Linac and a target chamber are kept under vacuum by using a Turbo Molecular Pump and Mechanical Fore Pump. The pressure is about 10^{-6} Torr. In the target chamber, there is a vertically movable target ladder on which the foil stacks are mounted. The target ladder position is monitored and controlled with circuits connecting to the Control Room. The detector system will be discussed in the next section.

3. Gas Flow System

The schematic diagram of the gas flow system for the proportional counter is shown in Fig. (3.4). Vacuum pump 1 and 2 operate throughout the experiment. If valve A is open with valves B and C closed, the pressure becomes the same at valve B,

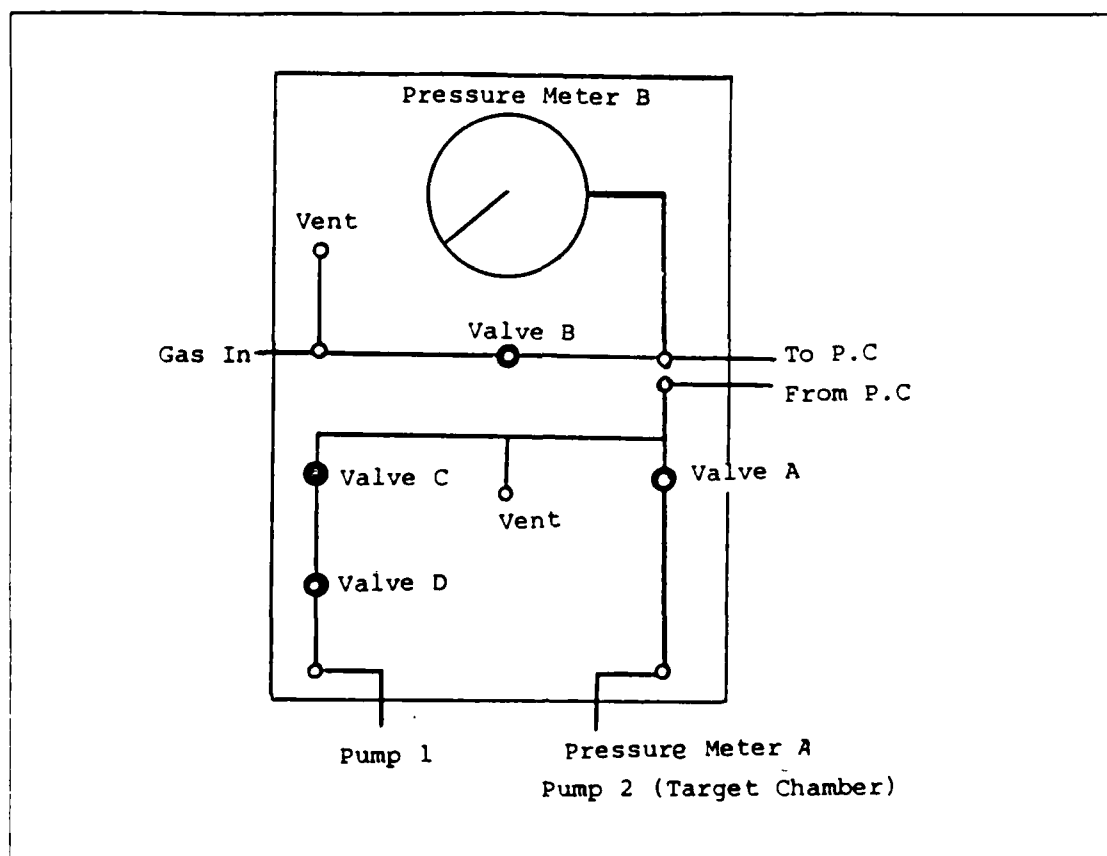


Figure 3.4 Schematic Diagram of a Gas Flow System.

C. and the proportional counter. Then, the target and the detector chamber are evacuated simultaneously through the valve A. Now close valve A and open valve C and D with the vacuum pump 1, 2 operating, and introduce argon and propane gas mixture to the proportional counter by opening the valve B. Set the valve C and D and valve B for stable gas pressure as required. The pressure meter B indicates the positive pressure with respect to the target chamber. Next supply a high voltage to the proportional counter and find the optimum pressure and voltage of the proportional counter.

4. Detection Apparatus

The reason for the use of the proportional counter [Fig. (3.5)] as a detector is that the low photon energy generates a few ion-electron pairs within this gas, and the generated pulses have a broad distribution reaching up to the amplifier noise level. For use in the soft x-ray region, between 100 eV and 3000 eV, the window of the

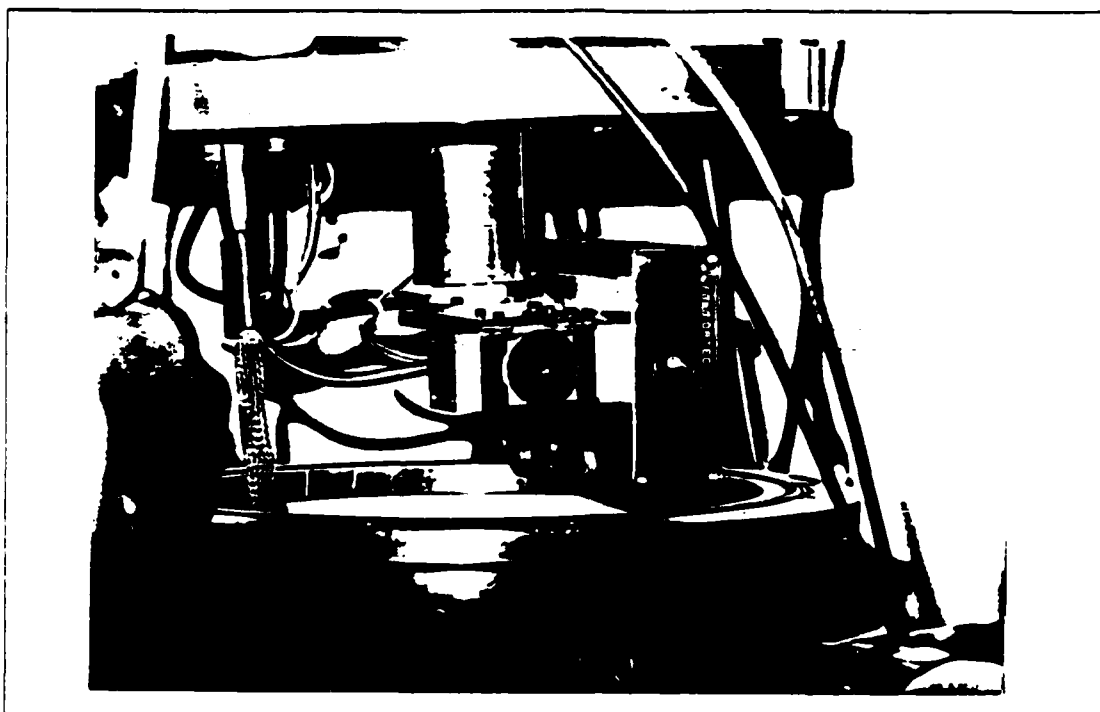


Figure 3.5 Detection Apparatus.

proportional counter must be quite thin and fragile. The mechanism of the proportional counter requires that the pressure of the gas be at least 40 Torr. The window forms a built-in filter which excludes stray electrons and ions from the detector and responses to the counter system [Ref. 10: p.1].

The window is made of VYNS (a copolymer of vinyl chloride and vinyl acetate). The composition is 5% H, 41% C, 5% O, 49% Cl by weight with a 55% transmission and 400 meshscreens having a 3×10 mm slot for operating maximum differential pressure of 800 Torr. For the proportional counter, the gas mixture of 90% argon and 10% propane (P-10 gas) is provided by the gas flow system and high voltage power (1200 V) is supplied. Use of the gas molecules as detection assures 100% photoionization yield above the ionization energy, and with zero yield below the ionization energy. The proportional counter gas is delivered from the tank which will provides a choice of several gas mixtures, allowing a change in primary detector medium by valving in the new gas. The performance depends strongly upon the gas pressure which can be controlled all the time during the experiment.

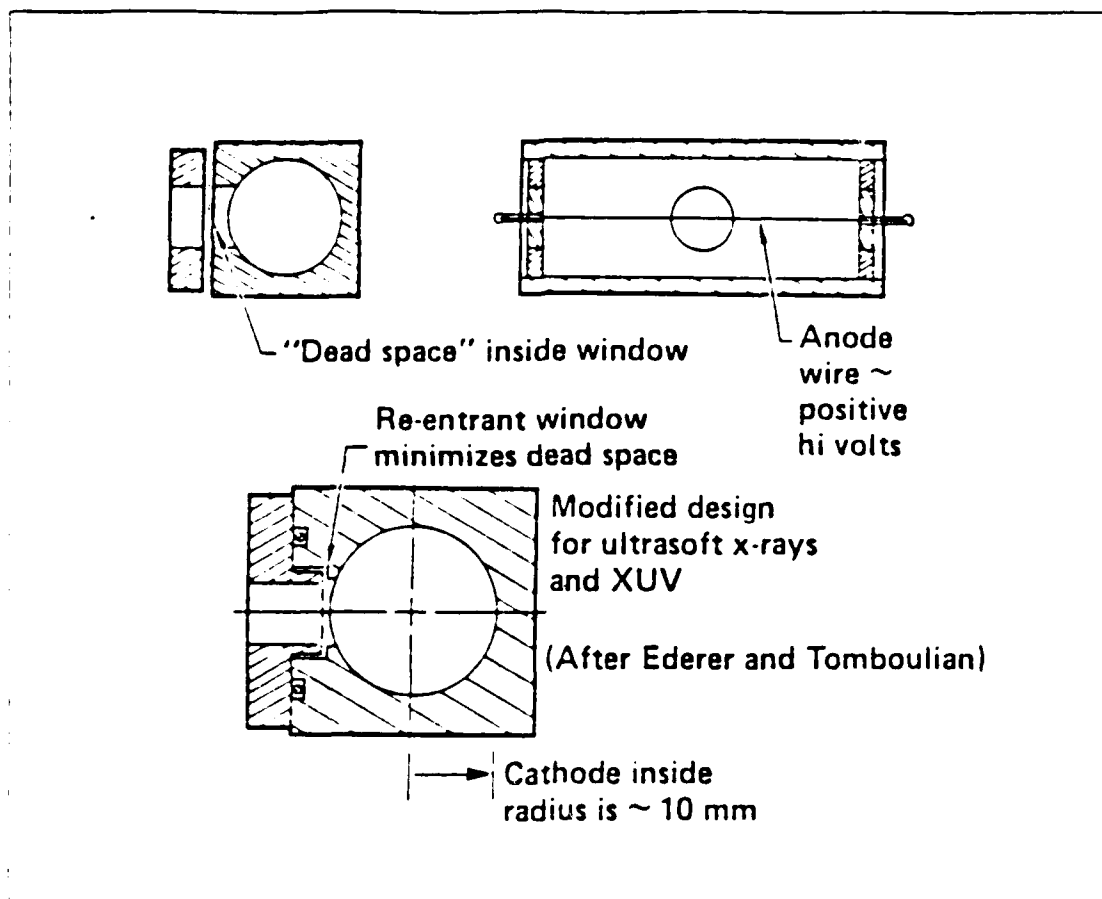


Figure 3.6 Manson Model 04 Gas Flow Proportional Counter.

The proportional counter provides information on the emitted photon energy of radiation being detected. The electronic analysis of the amplitude of the output pulse provides a technique for determining the photon intensity. Fig. (3.6) illustrates the basic design for the proportional counter. Since it is much easier to mount a flat-sided detector than a cylindrical detector, the proportional counter is designed as shown by boring the cylindrical hole in a rectangular cross section bar. The window can be mounted by clamping against the outside of the counter body.

Fig. (3.6) emphasizes the problem introduced by this mounting, that of the dead volume inside the detector. Ederer and Tomboulia introduced the design shown at the bottom in Fig. (3.6) for the use in the soft x-ray region. The reason for the concern with the dead space just behind the window is that the few electrons released in the initial absorption may be lost by diffusion back to the detector window. The

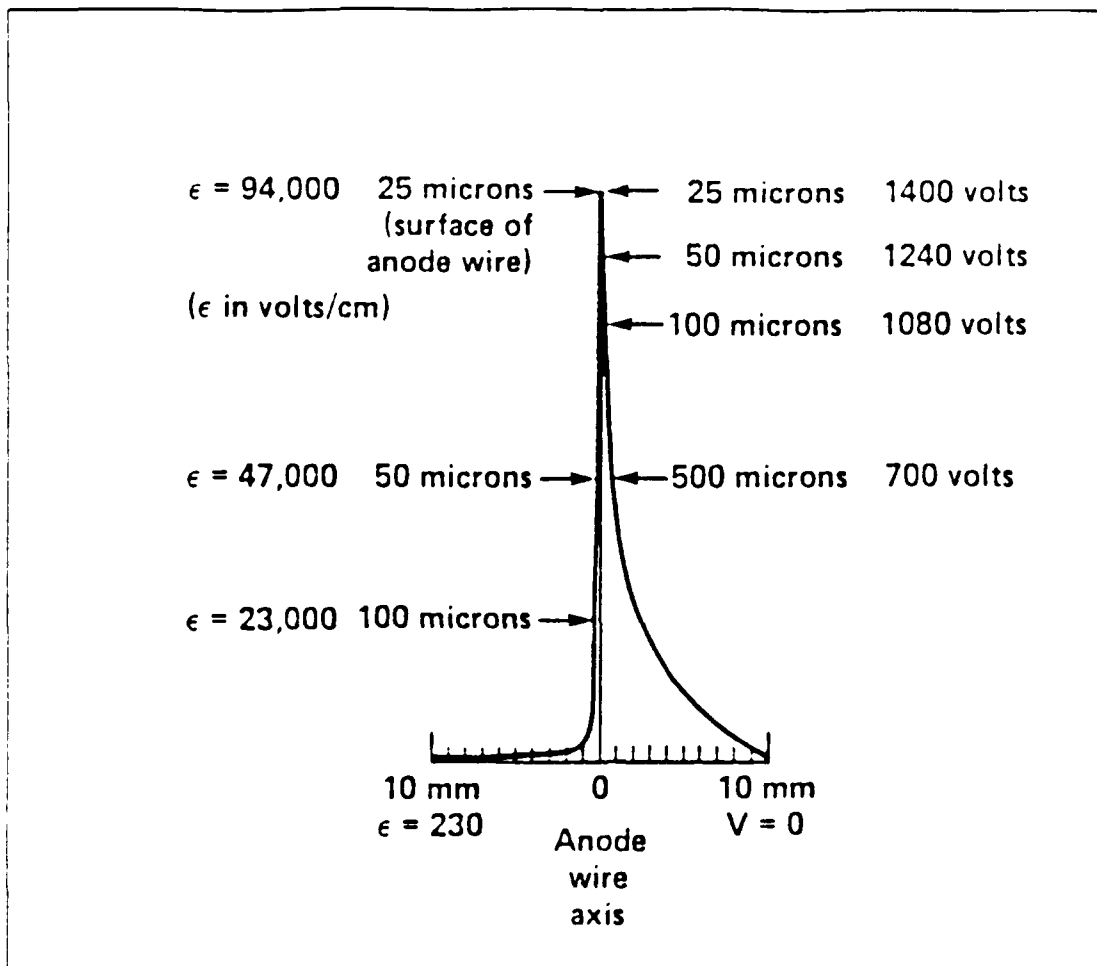


Figure 3.7 Electrical Field Strength and Potential vs. Radius.

counter used for the experiment has a stainless anode 50 μm in diameter, maintained at 1000 to 1500 volts positive potential. Fig. (3.7) shows the electric field and voltage distribution with respect to the location from the anode wire axis. The anode wire position is located at the center of the horizontal scale, which is a linear scale of radius measured from the axis of the counter running from the window at $r = 10 \text{ mm}$ at the left and the right. The field increases inversely proportional to the radius to very high values (94,000 V/cm) quite close to the anode wire [Ref. 10: p.3].

The initial event ion-electron pairs are separated rapidly by the field outside of the central region. When the electrons approach to within a few mean free paths of the anode wire, much energy is produced. At some radius, the energy gained by each

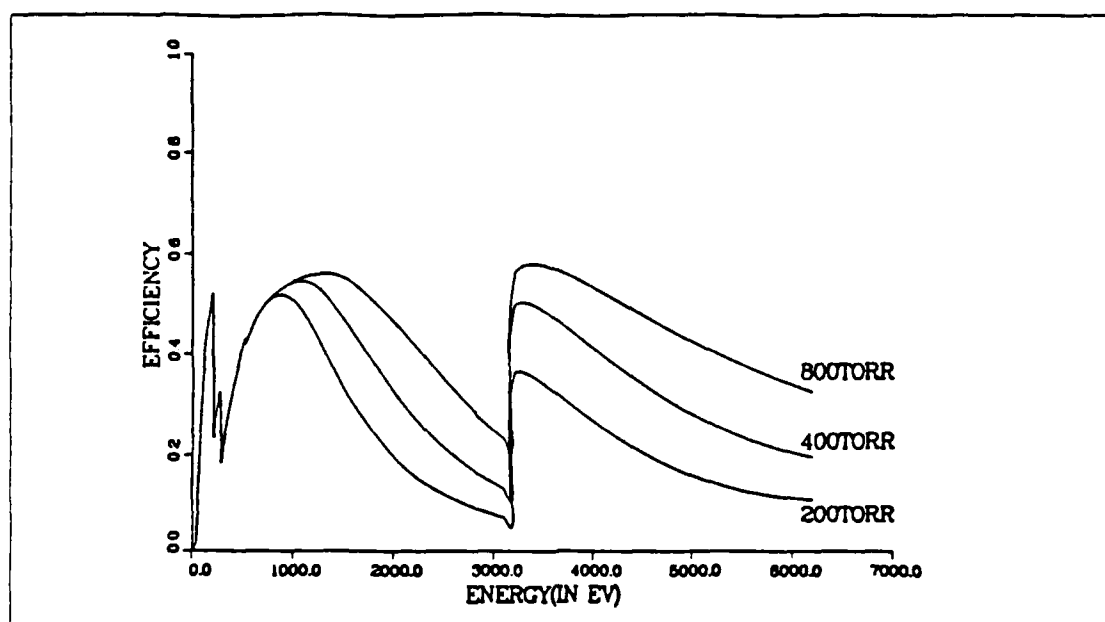


Figure 3.8 Proportional Counter Efficiency.

event electron between collisions is sufficient to cause secondary ionization. Between the collisions the energy increases as the radius decreases causing most of the ionization zone to be localized within $50 \mu\text{m}$ of the anode wire. The pulse induced on the central anode wire will be proportional to the potential difference through which the electrons and ions fall in their motions towards the wire and towards the grounded cathode inner surface. The positive ions move through most of the applied potential in their trip to the grounded cathode and this positive ion motion is the origin of the observed output pulse. Since part of the trip takes place in the very high field region near to the anode wire axis, the ion has a very high velocity through the steep potential gradient so the pulse starts off with a rapid initial rise, reaching about 50% of its maximum value within $0.5 \mu\text{s}$.

Fig. (3.8) shows the counter efficiency with respect to the photon energy. About 3.2 keV there is sudden change in efficiency, but the energy region of interest is below 3.2 keV. The proportional counter can be moved up and down by the driving motor, and the counter always points at the virtual center of the emission region.

5. Observation Station

The analyzing equipment consists of an ORTEC 142 PC preamplifier, an ORTEC 450 Research Amplifier, and a TRACER NORTHERN TN-7200 Pulse Height

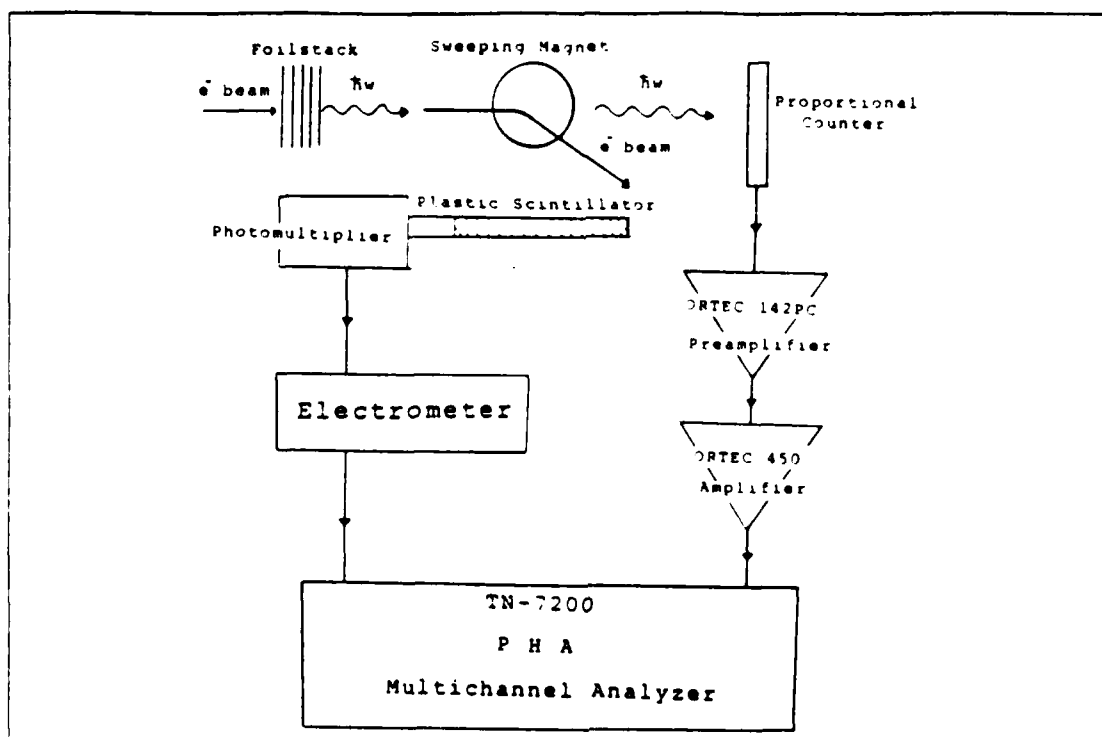


Figure 3.9 Block Diagram of the Data-collection Electronics.

Analyzer (PHA). The electron beam was deflected by the sweeping magnet through the large plastic scintillator which served as the beam monitor. The PHA received signal pulses from a charge-sensitive amplifier connected to the x-ray detector. Photons were counted until a fixed amount of beam charge had passed through the foil stack [Fig. (3.9)].

The PHA divides the detection range into a predetermined number of channels, and then records graphically the number of counts with which each signal channel is detected. The data is presented in the form of pulse height distribution with the number of counts per channel displayed on a linear vertical scale and the channel number displayed on a linear horizontal scale. The pulse-height is proportional to the incident photon energy. Thus the displayed results form an energy dispersed spectrum of the incident photon beam.

6. Stack Foils Used during Experiment

Two Al stack-foils and two Mylar stack-foils were used during the experiment. One aluminum stack has 30 foils with 1 μm foil thickness, the other has 1 foil of 26 μm

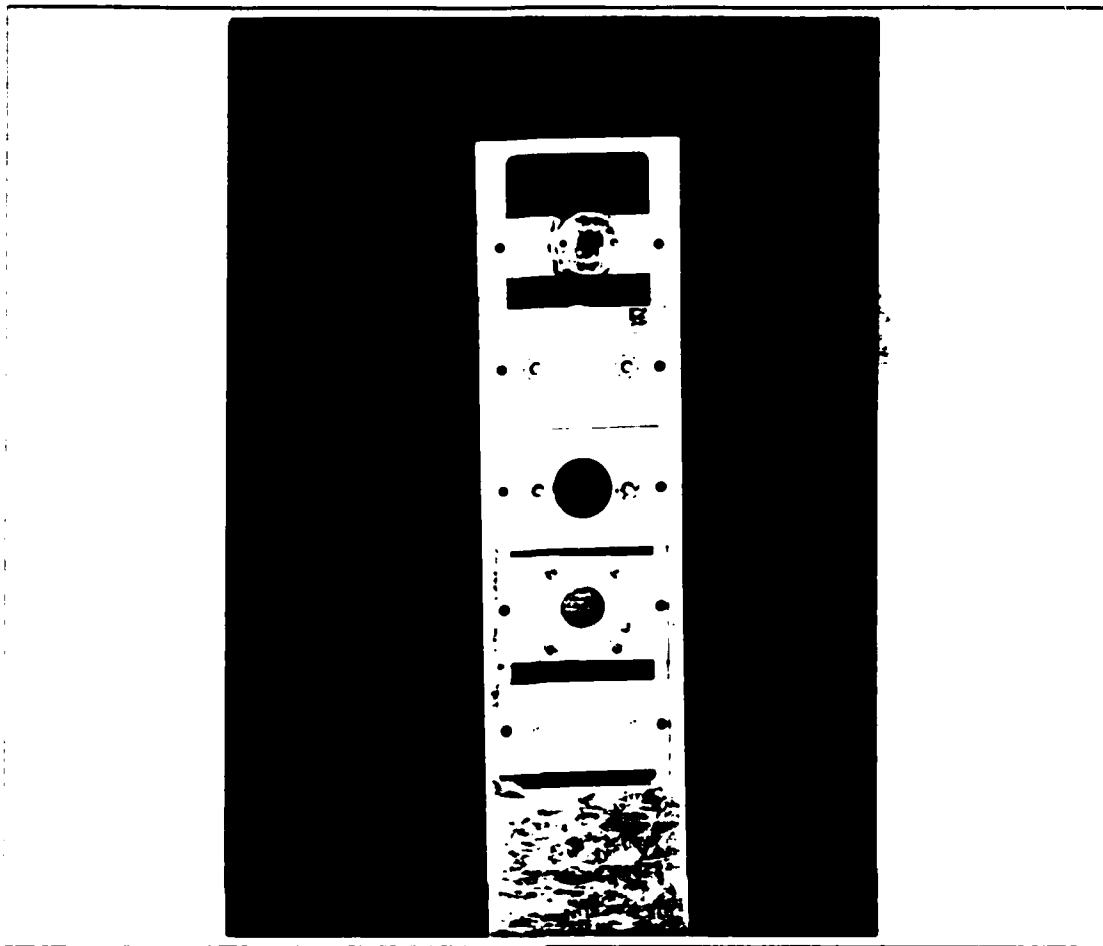


Figure 3.10 Stack Foils Used during Experiment.

foil thickness, one Mylar stack has 8 foils with $2.5\text{ }\mu\text{m}$ foil thickness, the other has 1 foil with $19\text{ }\mu\text{m}$ foil thickness. The Mylar foils were mounted on ladder 2.1-mm-stick ladder, while the Al foils were mounted on 1.5-mm-thick ladder. These dimensions were chosen to maintain adequate support of the delicate foils and keep the constant dimension [Fig. (3.10)].

A stack of 8 Mylar foils with each foil thickness $2.5\text{ }\mu\text{m}$ was constructed [Figs. (3.11) and (3.12)] in order to attain a coherent spectrum. This stack maintains a flat surface with a spacing 1.6 mm. Mylar was used because it is durable and does not tear easily when stretched.

The foil stacks produce both transition and bremsstrahlung radiation. To account for the bremsstrahlung background for each radiator, a single foil with

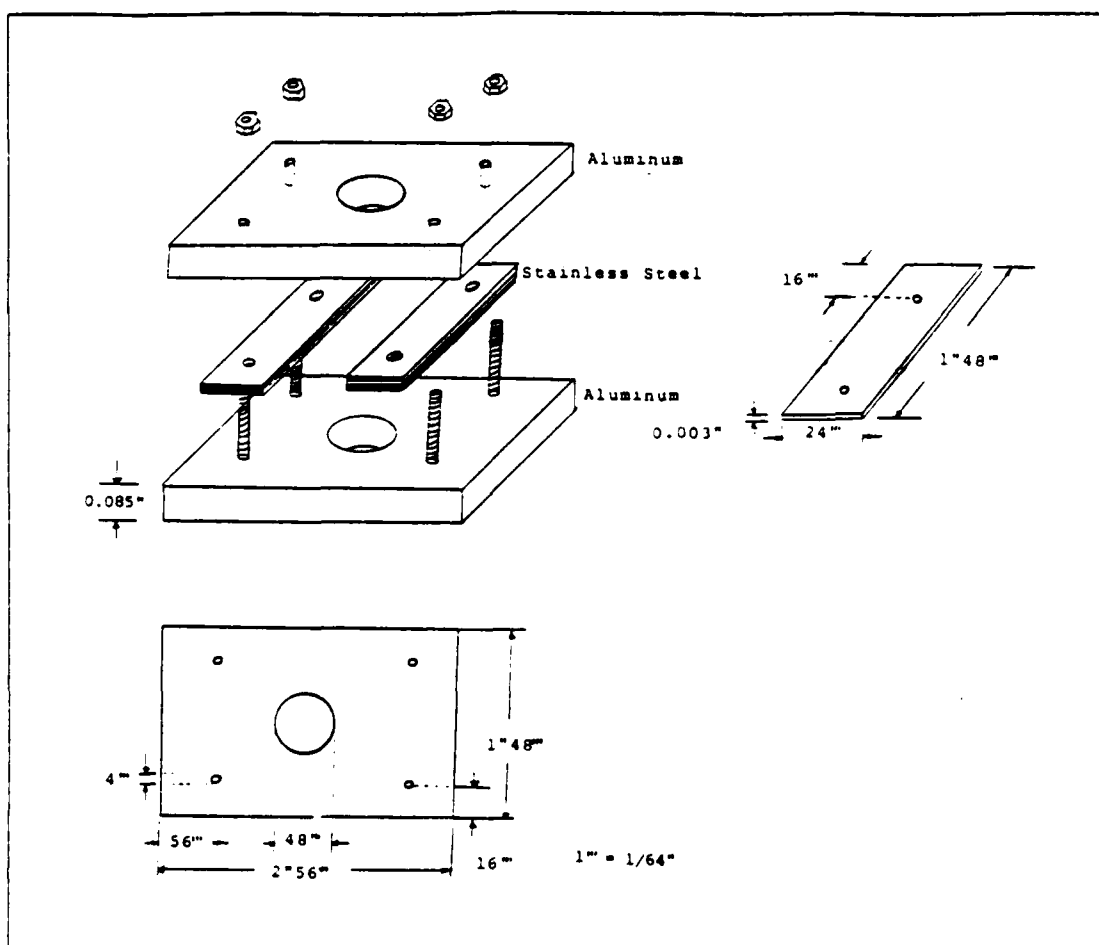


Figure 3.11 Design of Mylar Coherent Stack.

thickness equivalent to stack foils was constructed. The measured bremsstrahlung generated from the single foil using equal beam current was then subtracted from that produced by the corresponding foil stacks.

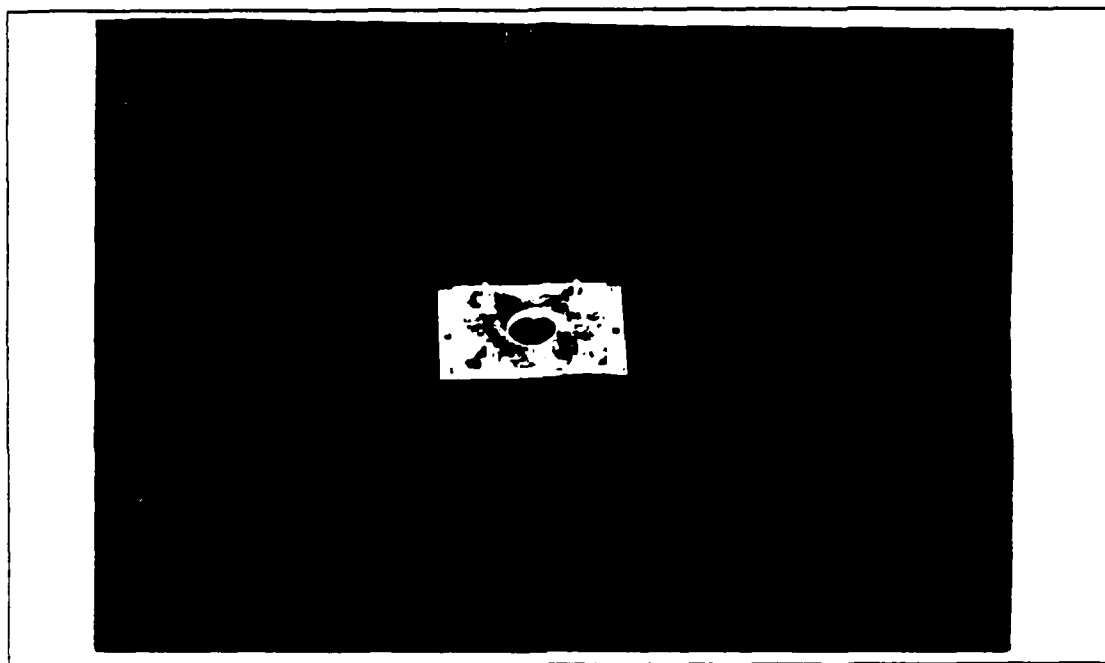


Figure 3.12 Mylar Coherent Stack.

IV. RESULTS AND CONCLUSIONS

A. RESULTS

Measurements of the total number of counts were carried out for several different positions of the detector. All measurements were for the same counting interval. The detector plane was 49" from the stack target. Motion of the detector was monitored by a counter with a scale of 0.0124" digit. The detector was on the beam axis at a scale reading of 335. Table 1 shows the total number of counts in region of interest for several different detector positions for 65 Mev electrons incident on 30 Al stack foils.

TABLE 1
MEASUREMENTS OF TOTAL COUNTS

Dial No.	Distance	Cone Angle	Counts No.
285	0.620"	12.65mr	10102
290	0.558"	11.39mr	10112
295	0.496"	10.12mr	10123
300	0.434"	8.86mr	10134
305	0.372"	7.59mr	10144
310	0.310"	6.33mr	10185
315	0.248"	5.06mr	10165

TABLE 2
COMPARISON OF RADIATION CONE ANGLE
AT 65 MEV

Optimum Angle	Measured Apex Angle
7.86mr	6.33mr

The error of the measured apex angle is ascribed to the discrete dial readings, the small dimensions of detector (1.8" x 3.8"), and electronics resolution.

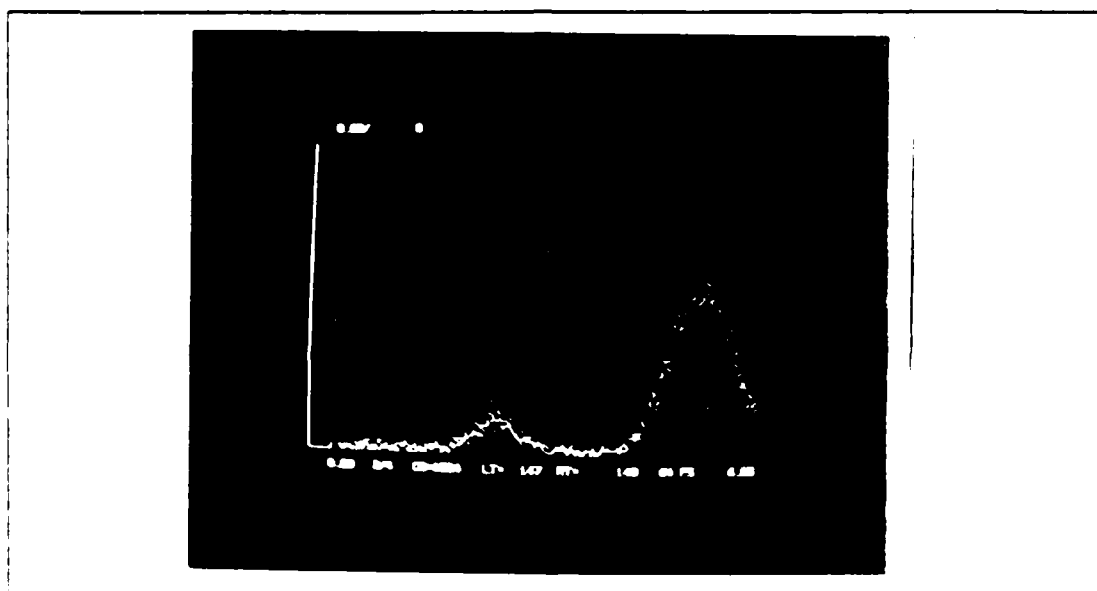


Figure 4.1 Fe^{55} Spectrum in 400 Torr.

The experimental results are shown in Fig. (4.1) through (4.6). Figs. (4.1) and (4.4) show the Fe^{55} spectra which have peaks at 3 and 5.9 keV. The experimental results for Al in Figs. (4.2) and (4.3) compare favorably with the theoretical predictions in Figs. (2.16) and (2.18) respectively. Similarly the experimental results for Mylar in Figs. (4.5) and (4.6) compare favorably with the theoretical predictions in Figs. (2.17) and (2.19) respectively. There is a good correspondence between the theoretical and

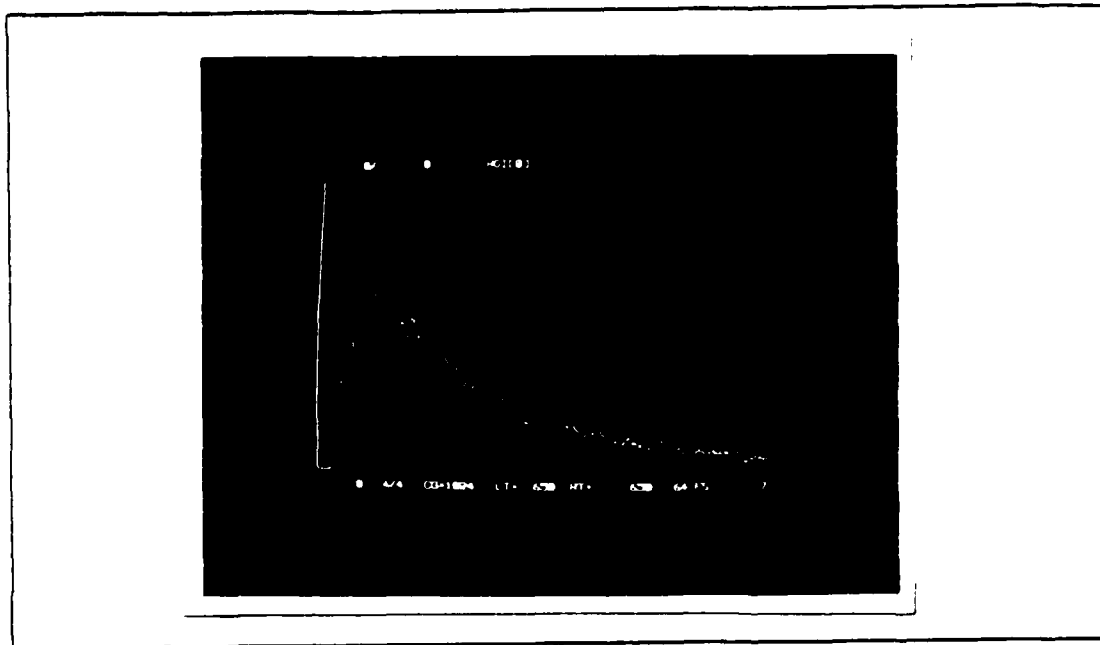


Figure 4.2 Measured Pulse Height Counts from 30 Foils $1\mu\text{m}$ Al with Bremsstrahlung.

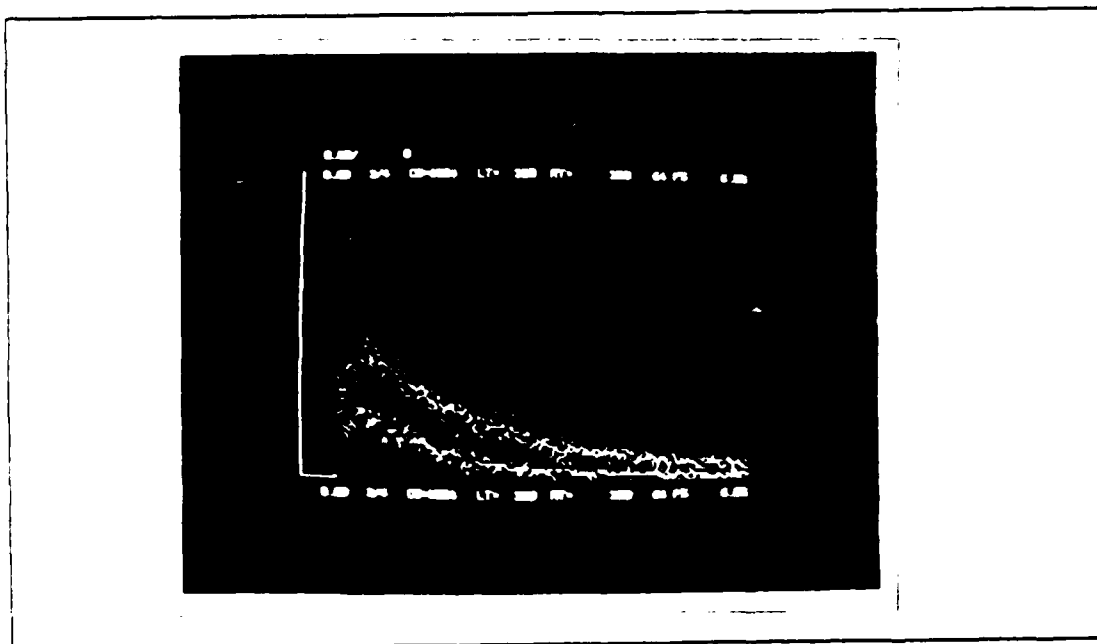


Figure 4.3 Comparison of Measured Pulse Height Counts from 30 Foils $1\mu\text{m}$ and 1 Foil $26\mu\text{m}$ Al.

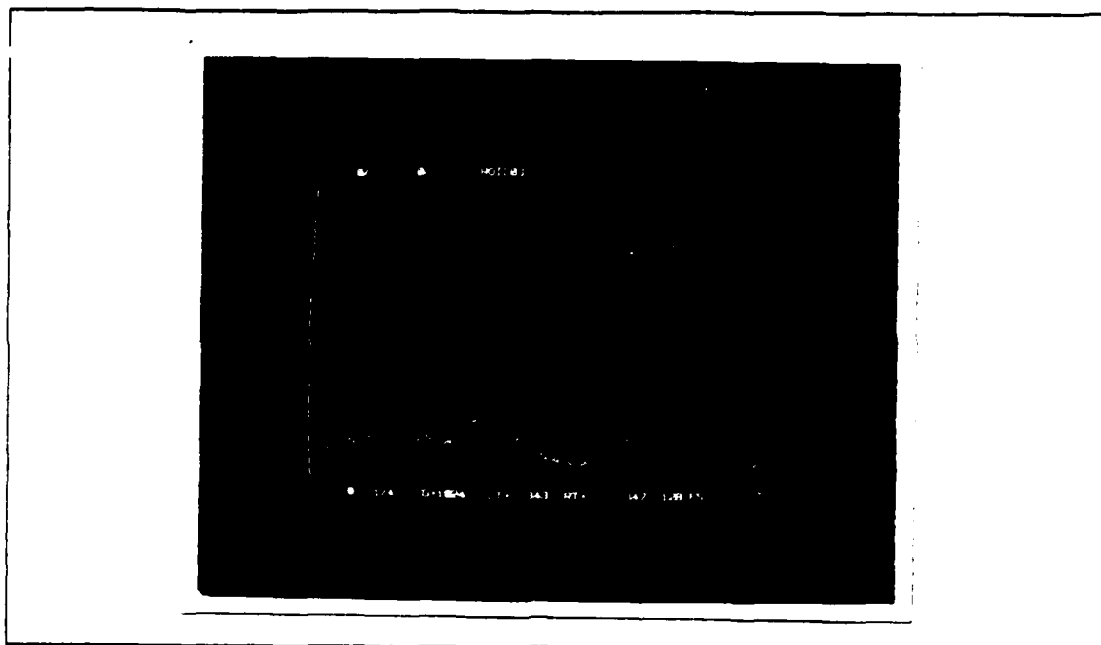


Figure 4.4 Fe^{55} Spectrum in 350 Torr.

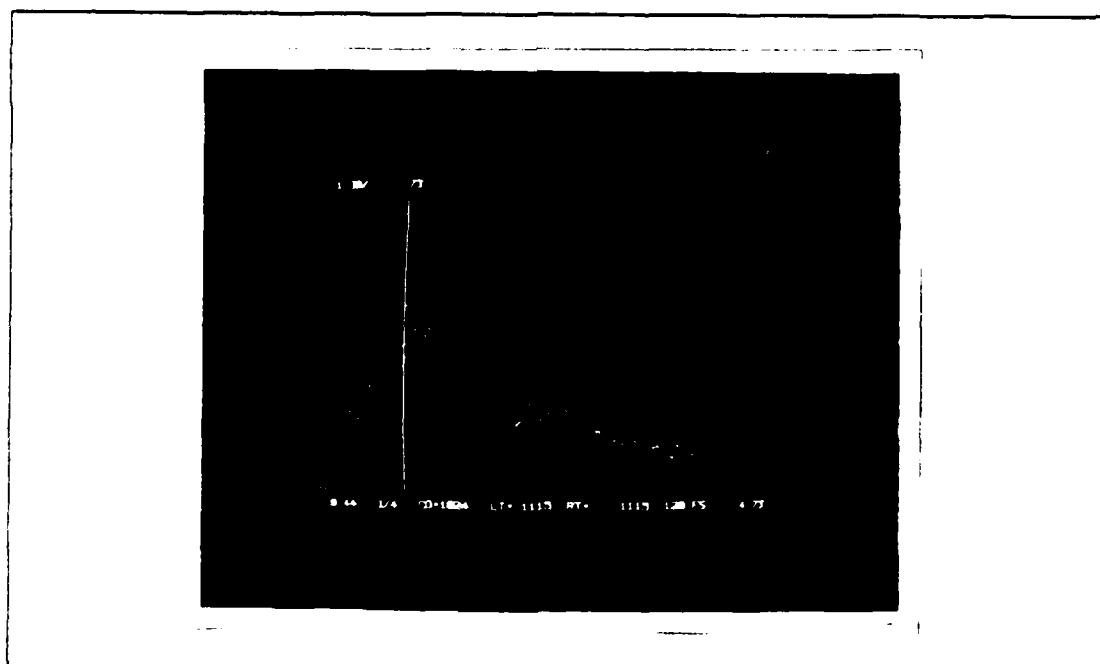


Figure 4.5 Measured Pulse Height Counts from 8 Foils $2.5\mu\text{m}$ Mylar with Bremsstrahlung.

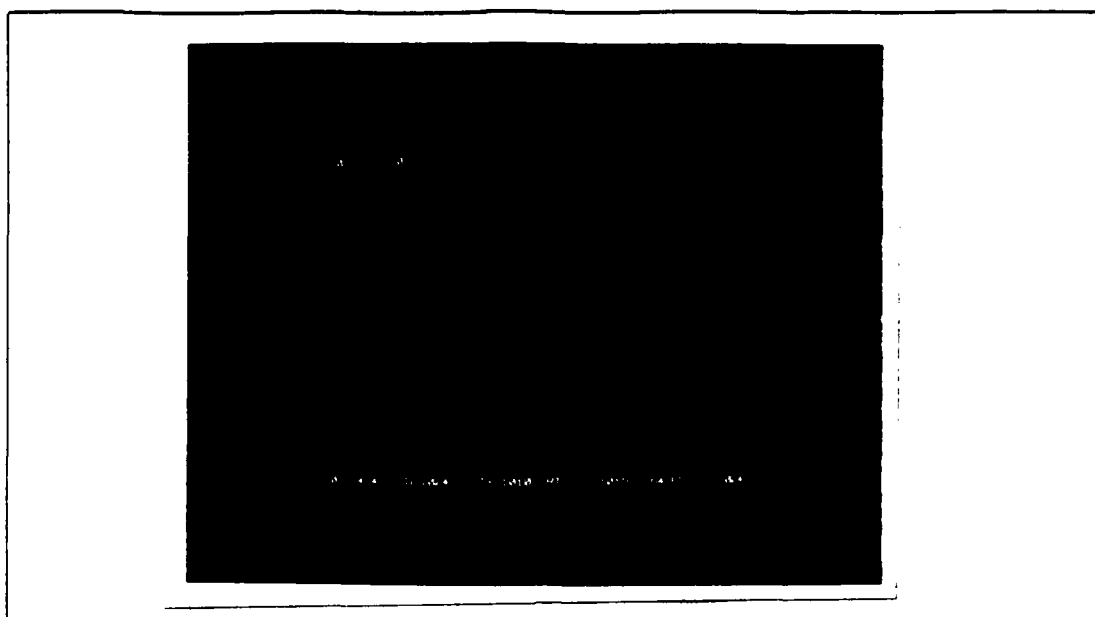


Figure 4.6 Measured Pulse Height Counts
from 1 Foil 19 μ m Mylar.

TABLE 3
COMPARISON BETWEEN CALCULATED AND MEASURED DATA

Foil	M	C.Peak	M.Peak	C.FWHM	M.FWHM
Al	30	1040 eV	1030 eV	1290 eV	1140 eV
Al	1	1000 eV	940 eV	1600 eV	1500 eV
Mylar	8	1330 eV	1380 eV	1580 eV	2200 eV
Mylar	1	1580 eV	1000 eV	1320 eV	1250 eV

* FWHM : the full width of the spectrum between points
having half the maximum production efficiency

the measured foil stack spectrum. The theoretical plots were calculated by using Eq. (2.16).

The ratio of the transition radiation to that of bremsstrahlung was 2.3 for Al and 2.7 for the Mylar foil. These ratios are lower than expected from the theory and the reason may be because there are other sources of background which were originally attributed to bremsstrahlung. A sudden change in intensity was observed at energy 3.1 keV for Mylar and it is due to the counter efficiency change from 0.2 to 0.5 [Fig. (3.8)].

Table 3 is a listing of four foil stacks, their respective number of foils, calculated peak frequencies, measured frequencies, calculated FWHM, and measured FWHM. For three of the foil stacks, the measured photon peak positions are found to agree with the calculated values. The single foil Mylar is noticeably different because of big fluctuations in small photon energy and of the modelling of unknown background. Comparison between the theoretical curves and their respective experimental measurements are limited to the position of the peak and the bandwidth. The measured FWHM energy for Al stack is reduced by 150 eV, and it is due to bandwidth narrowing associated with K-edge absorption ($E = 1.54$ keV).

B. CONCLUSIONS

The absolute differential production efficiencies (photons/eV sr electron) for soft x-rays emitted from each of four transition radiator were measured for incident electron-energy of 65 MeV. The radiators were made of stacks of 1.0- μ m-thick 30 foils Al, 25.4- μ m-thick single foil Al, 2.5- μ m-thick 8 foils Mylar, and 19- μ m-thick single foil Mylar. The radiation spectra were most intense between 0.6 and 1.8 keV for Al's, 0.9 and 3.1 keV for Mylar, peaking at 1.10, 1.00, 1.44, and 1.58 keV respectively.

The transition radiation cone was measured in different ways, and the measurement is in agreement with optimum apex angle. The radiation peak can be selected by proper selection of foil number, and thickness. For the case of foils separated by a vacuum, the peak frequency and bandwidth are dependent upon the foil thickness and plasma frequency. Measured peak energies correspond to the theory. Aluminum bandwidth narrowing associated with K-edge absorption was observed.

The highly directional beam, high photon production make an electron beam competitive as an x-ray source, especially for applications using a low energy, low current electron beam and requiring a small x-ray beam size. X-ray lithography, x-ray microscopy, and other medical application are possible.

However refinements remain to be done. Some specific suggestions are given below.

1. The magnet was used to deflect electrons from the photon path, but a part of them entered the photon path. They made noise. More powerful magnets are needed to eliminate electrons.
2. The experimental area was very noisy. It affected the observed spectrum. Noise could be decreased by electrically shielding the detector, which would decrease the electric field noise. Magnetic field noise associated with the LINAC klystrons could be reduced by thick concrete shielding.
3. The pipe through which photons pass is about 1.25", and the detector has the dimension 1/8"x3/8" of slotted window. The resolution smearing occurred by the shadow effect of photons. An x-ray detector with very fine resolution would be required.

Continued research of transition radiation include the following for future work:

1. Investigation of the effect of multi-foil scattering in transition radiation
2. Determination of the spectrum distribution of a radiator having the several different periodic media (such as Al, air, and Mylar)
3. Determine the dependency of the intensity and frequency spectrum on the resonance peak

APPENDIX A
ELECTRON LINEAR ACCELERATOR PARAMETERS

TABLE 4
LINAC PARAMETER

Max. Energy	120 MeV
Max. Average Current	20 μ amps
Length	9.14 m
Pulse Repetition Frequency	60 Hz
Pulse Width	1 μ s
Operation Frequency	2.856 GHz
Pulse Repetition Rate	120 PPS
Pulse Duration	2.5 μ s
Nr. of Klystron	3
Peak Power per Klystron	21 MW

APPENDIX B

CALCULATION OF PLASMA FREQUENCY

TABLE 5
PLASMA FREQUENCY

material	ω_p
Al	32.8 eV
Be	24.5 eV
Cu	54.6 eV
Mylar	19.9 eV

In the absence of a magnetic field, a plasma resonates electrostatically with the frequency. Ignoring the ion motion, the plasma frequency is given by

$$\omega_p = \sqrt{ne^2/\epsilon_0 m} \quad (2.1)$$

where e is 1.6×10^{-19} (coul), h is 1.055×10^{-34} (J.sec), m is 9.1×10^{-31} (kg), and $\epsilon_0 = 8.85 \times 10^{-12}$ (F.m). Substituting these values into Eq. (2.1), the plasma frequency becomes

$$h\omega_p = \sqrt{n} \cdot 3.718 \times 10^{-11} \text{ (eV)} \quad (2.2)$$

The electron concentration can be obtained by

$$n = ZNp/A \quad (2.3)$$

where n is the number of electrons per cm^3 , Z is atomic number, N is avogadro number, ρ is density (gm/cm^3), and A is atomic weight. For Al $n = 7.8 \times 10^{23}$ (electrons/ cm^3), the plasma frequency has the value $\hbar\omega = 32.84$ (eV).

APPENDIX C

MASS ATTENUATION COEFFICIENTS FOR PHOTONS IN AL AND MYLAR

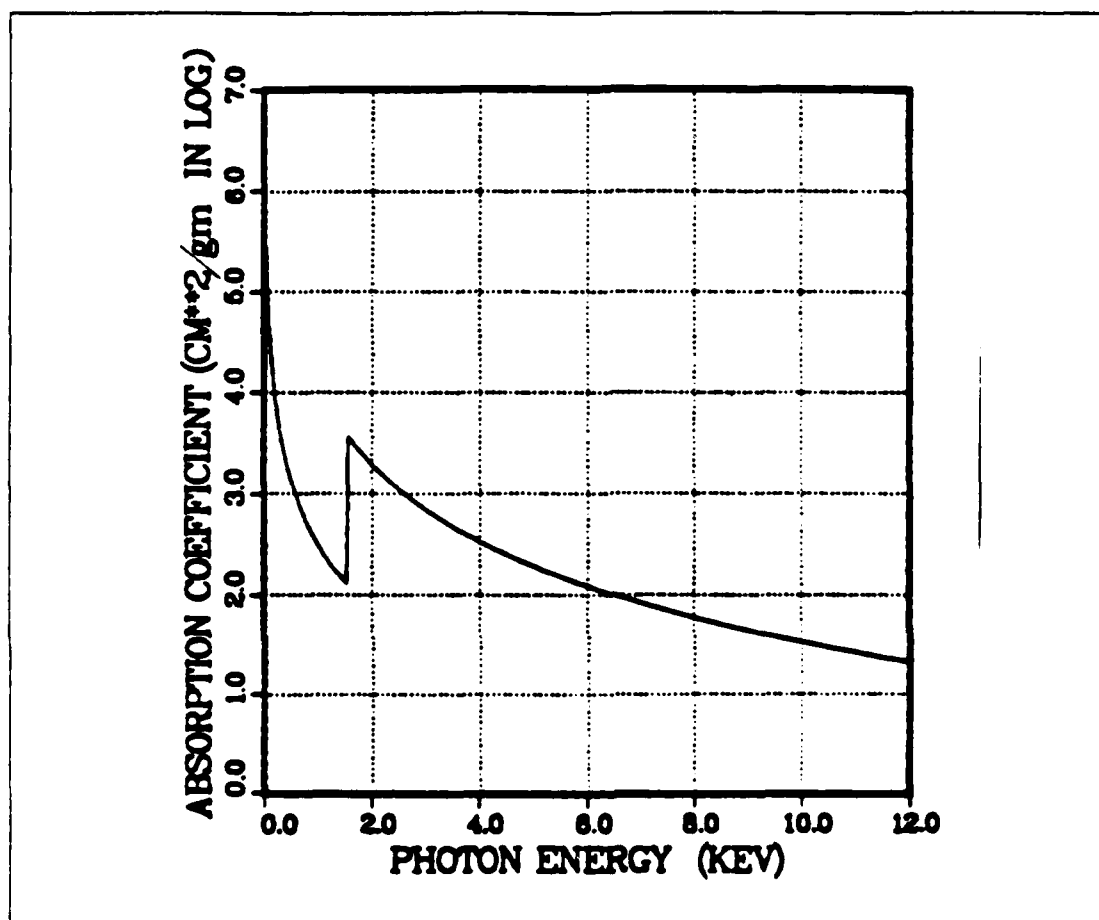


Figure C.1 Mass Attenuation Coefficient for Photons in Al.

Corresponding linear coefficients for Al can be obtained by multiplying all curves by $\rho = 2.70 \text{ (g cm}^3\text{)}$ for Al [Fig. (C.1)] and $\rho = 1.395 \text{ (g cm}^3\text{)}$ for Mylar [Fig. (C.2)] (at $T = 0^\circ\text{C}$, $P = 760 \text{ mmHg}$). Mylar ($\text{C}_5\text{H}_8\text{O}_2$) mass attenuation coefficients are obtained approximately by taking $\mu \rho = 1.3(\mu \rho)_\text{O} + 5.8(\mu \rho)_\text{C}$.

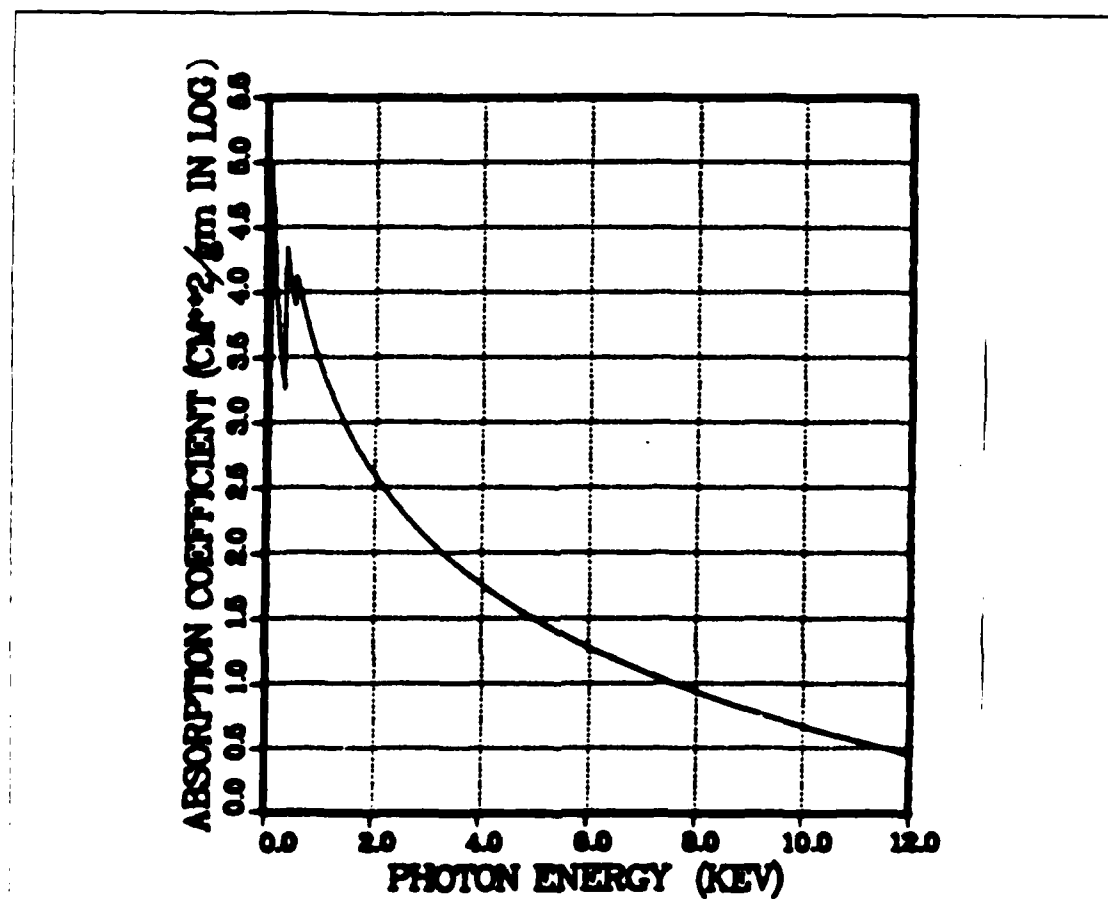


Figure C.2 Mass Attenuation Coefficient for Photons in Mylar.

APPENDIX D

BASIC PROGRAM (HP COMPUTER)

```

***** INFORMATION *****
* THE OBJECTIVE OF THIS PROGRAM IS TO CALCULATE AND DRAW *
* THE ABSOLUTE DIFFERENTIAL PRODUCTION EFFICIENCIES FROM *
* STACK MATERIAL. THE DRAWING METHOD IS THE FUNCTION *
* CURVE OF DISSPLA. *
***** VARIABLE DEFINITION *****
* L : FOIL THICKNESS IN  $\mu$ m *
* X : ENERGY IN KEV *
* K : ENERGY IN FREQUENCY *
* D : ABSOLUTE COEFFICIENT *
* Y : MULTI-FOIL ABSORPTION COEFFICIENT *
* O : PLASMA FREQUENCY IN KEV *
* A : PLASMA FREQUENCY IN FREQUENCY *
* N,AA,B : SINGLE INTERFACE FACTOR *
* U : FORMATION LENGTH Z1 *
* G,E : FORMATION LENGTH Z2 *
* F : SINGLE FOIL FACTOR *
* GG,H : TOTAL PRODUCTION EFFICIENCY *
* M : TOTAL ABSORPTION FACTOR *
***** VARIABLE DEFINATION *****
C-----
C A PROGRAM FOR PLOTTING BY SHERPAOR BY TEK618
C-----
C GRAPH OF XY DATA GIVEN
C PROGRAM GRF2D
C CALL TEK618
C CALL PRTPLOT
C CALL XYPLOT
C CALL DONEPL
C STOP
C END
C PLOTTING THE GIVEN FUNCTION
C SUBROUTINE XYPLOT
C-----
C MAIN PROGRAM
C-----
C DIMENSION X(300),Y(300),D(300),K(300),A(300),B(300),C(300),E(300)
C DIMENSION F(300),G(300),H(300),M(300),L(300),N(300),O(300),P(300)
C DIMENSION Q(300),R(300),S(300),T(300),U(300),V(300),W(300),AA(300)
C DIMENSION BB(300),CC(300),FF(300),EE(300),GG(300),YY(300)
C REAL X,Y,D,K,A,B,C,E,G,H,M,L,Z,N,O,P,Q,R,S,T,U,V,W,AA,BB,CC,FF,GG
C REAL YY
C INTEGER I,J
C CALL PAGE(12.,9.)
C CALL AREA2D(9.,5.9)
C CALL AREA2D(5.5,6.)
C CALL YAXANG(90.)
C CALL XASANG(0.)
C CALL MX2ALF('L/CSTD','/')
C CALL MX3ALF('ITALIC','%')
C CALL HEIGHT(0.2)
C CALL XNAME('PHOTON ENERGY (KEV)',20)
C CALL XNAME('NUMBER OF FOIL',14)
C CALL YNAME('PHOTONS / EV/STERAD./ELECTRON) 10**(-4)',39)
C CALL YNAME('SINGLE INTERFACE * MULTI-FOIL AB. 10**(-8)',42)
C CALL YNAME('ABSORPTION COEFFICIENT (CM**2 /GM) IN LOG',41)
C CALL YNAME('MULTI-FOIL INTERFERENCE FACTOR',30)
C CALL COMPLX
C CALL HEADINI('PRODUCTION EFFICIENCY',21,2.5,1)
C CALL HEADINI('MULTI-FOIL INTERFERENCE',23,1.5,1)
C CALL RESET('HEIGHT')
C CALL FRAME
C CALL CROSS
C CALL GRAF(0.,100.,600.,0.,100.,500.)
C CALL DOT
C CALL GRID(1,1)
C CALL RESET('ALL')
C CALL POLY3
C CALL THKCRV(.05)
C CALL MARKER(1)

```

```

CALL HEIGHT(.15)
Z = 0.
DO 30 J = 1,5
  Z = Z + 1
  DO 20 I = 1,300
    M(I) = 4*Z
    L(I) = 1
    X(I) = FLOAT(I)/25
    K(I) = 1.51659*X(I)
    D(I) = 3.91-0.39*X(I)
    D(I) = 5.55-X(I)*0.55
    D(I) = LOG10(X(I))
    EE(I) = -2.1*LOG10(X(I))+2.5
    FF(I) = -3.0792*LOG10(X(I))+3.7024
    D(I) = 10*(EE(I))*0.003*2.7
    EE(I) = -2.1*LOG10(X(I))+2.5
    D(I) = 10*(EE(I))*1*1E-4*2.7
    D(I) = 0.001
    Y(I) = 1/D(I)*(1-EXP(-X(I)*D(I)))
    O(I) = 30.9E-3
    A(I) = 1.51659*O(I)
    B(I) = 1.8282E-7*K(I)**(-5)*A(I)**4
    C(I) = 1.236E-4*(A(I)/K(I))**2
    E(I) = 1/K(I)*1.2E9/C(I)
    U(I) = 6.4E-6/X(I)
    W(I) = (U(I)-E(I))*1E-18**2
    AA(I) = 3.174E-26*W(I)*K(I)*1E18*1.5172E15*1E4**4
    F(I) = SIN(L(I)*1E-6/E(I)*1E18)**2
    G(I) = 80*0.6/(1.236E-4*(A(I)/K(I))**2)
    H(I) = G(I)**2*F(I)*B(I)*Y(I)*1E-18*1.523E15
    M(I) = Y(I)*F(I)
    P(I) = 1.236E-4*(1.236E-4*(O(I)/X(I))**2)
    N(I) = 1.8282E-25*O(I)**4*X(I)**(-5)*P(I)**(-2)*1E17
    T(I) = 3175/U(I)+L(I)/E(I)*1E12
    Q(I) = (SIN(8*T(I))/SIN(T(I)))**2
    T(I) = L(I)/E(I)*1E12
    Q(I) = 1+EXP(-8*D(I))-2*EXP(-4*D(I))*COS(16*T(I))
    R(I) = 1+EXP(-D(I))-2*EXP(-D(I)/2)*COS(2*T(I))
    S(I) = Q(I)/R(I)
    GG(I) = AA(I)*Y(I)*F(I)
    CC(I) = AA(I)*S(I)
    BB(I) = AA(I)*F(I)*Y(I)
    V(I) = N(I)*F(I)*S(I)*1.523E15
    WRITE(6,55)X(I),GG(I)
55  FORMAT(' ',4E10.3)
    READ(6,55)X,Y1,Y2
55  FORMAT(D11.3,2X,2D12.3)
20  CONTINUE
CALL CURVE(X,Q,300,0)
CALL ENDGRIO)
30  CONTINUE
CALL RESET('ALL')
CALL ENDPLIO)
CALL ENDGRIO)
RETURN
END

```

LIST OF REFERENCES

1. I. M. Frank and V. L. Ginzburg, "Radiation of a Uniform Moving Electron due to Its Transition from One Medium into Another," *Journal of Physics*, vol. 9, May 1945.
2. M. L. Cherry, G. Hartman, D. Muller, and T. A. Prince, "Transition Radiation from Relativistic Electrons in Periodic Radiators," *Physics Review D*, vol. 10, December 1974.
3. G. B. Yodh, "State of the Art of Transition Radiation Detectors," *IEEE Transaction on Nuclear Science*, vol. NS-31, 1984.
4. A. N. Chu, M. A. Piestrup, T. W. Barbee, Jr., and R. H. Pantell, "Transition Radiation as a Source of X-rays," *Journal of Applied Physics*, vol. 51, March 1980.
5. M. A. Piestrup, J. O. Kephart, H. Park, R. K. Klein, and R. H. Pantell, "Measurement of Transition Radiation from Medium-energy Electrons," *The American Physical Society*, vol. 32, no. 2, August 1985.
6. M. L. Ter-Mikaelian, *High Energy Electromagnetic Process in Condensed Media*, New York, Wiley-Interscience, 1972.
7. J. D. Jackson, *Classical Electrodynamics*, John Wiley and Sons, Inc., New York, 1975.
8. A. N. Chu, M. A. Piestrup, P. F. Finman, R. H. Pantell, and R. A. Gearhart, "A Source of X-rays Using Resonance Transition Radiation," *IEEE Transaction Nuclear Science*, vol. NS-29, February 1982.
9. Michael L. Cherry, Gernot Hartmann, Dietrich Muller, and Thomas A. Prince, "Transition Radiation from Relativistic Electrons in Periodic Radiator," *Physical Review D*, vol. 10, no. 11 December 1974.
10. Manson, J. E. *Instructions for Model 04 Photon Counter*, Private Communication, February 1984.

INITIAL DISTRIBUTION LIST

	No. Copies
1. Defense Technical Information Center Cameron Station Alexandria, Virginia 22304-6145	2
2. Library, Code 0142 Naval Postgraduate School Monterey, California 93943-5002	2
3. Physics Library, Code 61 Department of Physics Naval Postgraduate School Monterey, California 93943-5000	1
4. Professor J. R. Neighbours, Code 61Nb Department of Physics Naval Postgraduate School Monterey, California 93943-5000	2
5. Professor F. R. Buskirk, Code 61Bs Department of Physics Naval Postgraduate School Monterey California 93943-5000	2
6. Library Korea Military Academy Gong-reung-dong 556-21 Republic of Korea 130-02	1
7. Yoon, Seog Koo 476 Sang-sa, Rack-sung-ri, Kum-gu-myon Kim-je-gun, Jeon-buk Republic of Korea 550-16	11
8. Jung, Yun Su SMC 2643 Naval Postgraduate School Monterey California 93943-5000	1
9. Lee, Young Moon SMC 1110 Naval Postgraduate School Monterey California 93943-5000	1
10. Wee, Kyoum Bok SMC 2814 Naval Postgraduate School Monterey California 93943-5000	1
11. Yoon, Sang Il SMC 1558 Naval Postgraduate School Monterey California 93943-5000	1

END

5-87

DTIC